# INVESTIGATION OF THE GEM MPD THRUSTER USING THE MACH2 MAGNETOHYDRODYNAMICS CODE

BY

DREW AHERN

THESIS

Submitted in partial fulfillment of the requirements
for the degree of Master of Science in Aerospace Engineering
in the Graduate College of the
University of Illinois at Urbana-Champaign, 2013

Urbana, Illinois

Adviser:

Professor Rodney L. Burton

# Abstract

This work investigated using the MACH2 plasma simulation code in replicating the results of previous experimental work on the gallium electromagnetic (GEM) thruster. MACH2 was also used to examine possible changes to the GEM thruster that could improve the performance of the actual thruster. Thruster radius ratios of 3.4 and 5 were examined, and a mass flow rate of 6 g/s was specified for each. In this study, several properties were examined and compared with the experimental GEM thruster. A voltage of 148 V was computed for the GEM thruster with a radius ratio of 3.4, and a voltage of 222 V was computed for a thruster with a radius ratio of 5. Electron density and axial velocity values were analyzed and compared with experimental data. The simulated magnetic field near the cathode was shown to be very close to experimental measurements. Pressure simulation results were assessed, which indicated the presence of an electrothermal thrust component. Temperatures were observed and compared, and the electrical conductivity was examined. A momentum flow rate parameter was derived to examine thrust values, and results of 124 N and 131 N with thruster efficiencies of 38% and 28% were calculated for the radius ratios of 3.4 and 5, respectively. Additionally, plasma heating was found to dominate in the region near the cathode surface.

## Acknowledgements

I would like to thank my advisor, Dr. Rodney Burton, for his help and support on this project. I am very grateful for his expertise, as his advice greatly helped in narrowing down solutions to problems and obtaining tenable results. I am also indebted to Dr. Jason Cassibry at the University of Alabama in Huntsville for meeting with me personally to help me understand the MACH2 code, as well as for his generosity in taking the time out of his busy schedule to talk with me and answer questions via phone and email. This work would not have been possible without his help. I would also like to thank the Aerospace Engineering Department at the University of Illinois for my fellowship and support. Additionally, I would like to thank Diane Jeffers and the Illinois Space Grant Consortium for helping fund my trip to the University of Alabama in Huntsville. Regarding the MACH2 code, I would like to thank David Amdahl at the Kirtland Air Force Base for helping me install and set up the code. Last but not least, I would like to thank my parents for their love and support.

# Table of Contents

# Nomenclature

$\eta$ – efficiency

$\mu_0$ – vacuum permeability

ρ – density

$B_\theta$ – azimuthal magnetic field

BC – boundary condition

C – path of integration or constant relating to geometry of cathode

**E** – electric field

$F_z$ – MPD thruster predicted axial force

$F_{z,cathode}$ – force due to pressure on cathode

$F_{z,axial}$ – axial momentum flow rate

$F_{z,radial}$ – radial momentum flow rate

$F_{z,total}$ – total momentum flow rate

g – gravitational constant, 9.81 m/s$^2$

GEM – gallium electromagnetic

h – height of cell

$h_e$ – specific enthalpy due to electrons

$h_i$ – specific enthalpy due to ions

$h_{total}$ – total specific enthalpy

I – current

$I_{sp}$ – specific impulse

**j** – current density vector

**j** x **B** – Lorentz body force

$\dot{m}_{axial}$ – axial mass flow rate

$\dot{m}_{radial}$ – radial mass flow rate

$\dot{m}_{total}$ – total mass flow rate

MACH – Multiblock Arbitrary Coordinate Hydromagnetic

MPD – magnetoplasmadynamic

PFN – pulse forming network

r – radius, radial coordinate, or leftmost radius value

$r_a$ – anode radius

$r_c$ – cathode radius

R – cell rightmost radius value

RR – radius ratio

$T_e$ – electron temperature

$T_i$ – ion temperature

$U_e$ – exhaust velocity

v – axial velocity at cell corner

V – voltage

$V_{axial}$ – midpoint axial velocity

$V_{radial}$ – midpoint radial velocity

z – axial coordinate

Z – ion charge state

# Chapter 1 Introduction

## 1.1 MPD Thrusters

The magnetoplasmadynamic (MPD) thruster is a high power electric propulsion method which functions by accelerating ionized plasma through a magnetic field, producing a thrust force. A typical device consists of two coaxial electrodes and a discharge chamber between the two through which a gas propellant flows. A high current arc (on the order of several tens of kA) passes through the electrodes, inducing an azimuthal magnetic field between the electrodes, while also creating an ionized plasma. The current density and magnetic field interact via the Lorentz force through the volume of the discharge chamber, generating a thrust [1, 2]. A typical MPD thruster is shown below in Figure 1.1.

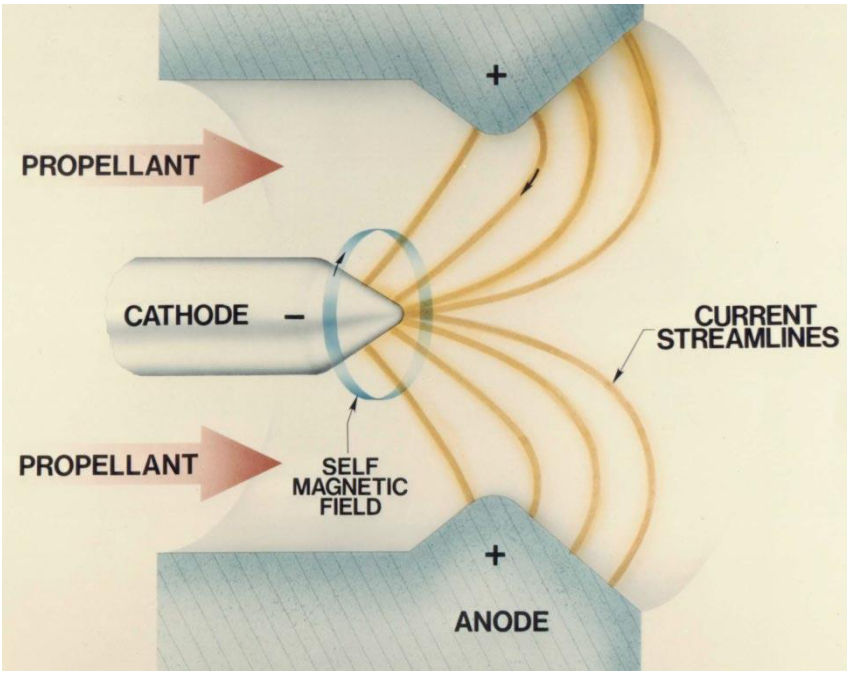


Figure 1.1: Typical MPD thruster [3].

In terms of performance, MPD thrusters have been shown to have a specific impulse ($I_{sp}$) in the range of 1,000 to over 10,000 s. Efficiencies have been measured at 55% (with $I_{sp}$ = 6,000 s)

using lithium propellant and 50% (with $I_{sp}$ = 15,000 s) using hydrogen propellant. Further increases in performance have been predicted through optimizing mass flow properties and thruster geometry [4]. Compared to other electric propulsion methods, the MPD thruster has a relatively high thrust per unit area ratio, requiring fewer thrusters on a space mission and thus a lower overall complexity [5].

### 1.2 MPD Thruster Systems Issues

One downside of the MPD thruster is electrode erosion, as the high current causes evaporation of the cathode. This result limits the overall lifetime of the thruster, where lifetimes of 5,000 hours are necessary for space missions [4]. In addition, it has become evident that the MPD thruster must be pulsed at a high rate (up to several hundred Hz) in order to reduce the size of the capacitor storage bank. This requirement, in turn, requires a fast way of injecting mass pulses into the thruster that are synchronous with the current pulses. The GEM thruster is an approach that addresses these issues to create a low mass, reliable, high-power electric propulsion system.

### 1.3 GEM Thruster

The gallium electromagnetic (GEM) thruster is an MPD thruster that was conceived at the Marshall Space Flight Center and more recently has been under development at the University of Illinois [5-8]. The main difference between the GEM thruster and a typical MPD thruster is that instead of a gas propellant, the GEM thruster uses a central gallium electrode that functions both as the cathode and as the propellant. This occurs through the high current arc ablating the gallium cathode, which produces ionized plasma.

There are several advantages to this design. Foremost, lifetime issues are mitigated through the electrode erosion becoming an integral part of the design; the gallium acts as both a conduction

path and a propellant. Additionally, typical gas-fed MPD thrusters require pulsed valves to operate, which become unreliable at high temperatures for pulse numbers on the order of $10^{10}$ pulses [6]. The GEM thruster, however, does not require these pulsed valves since the gallium ablation is the propellant injection. Furthermore, experimental ground-based test facility vacuum pump requirements for the GEM thruster are less than those for gas-fed MPD thrusters. In terms of propellants, the use of gallium is advantageous as it is non-toxic and can be safely handled. It also has a high density, which results in low storage volume requirements, and it becomes liquid at 30°C.

### 1.4 MACH2 Code

The plasma simulation code MACH2, short for Multiblock Arbitrary Coordinate Hydromagnetic, was used in this study to simulate the GEM thruster. MACH2 has been used in the past for simulating various electric propulsion thrusters. MPD thrusters have been simulated previously, however these have typically used hydrogen or argon as a propellant [9-12] – an ablative cathode design was not used. In terms of ablation, several studies have been performed [13-15], though not on MPD thrusters. A MACH2 study has been performed on the GEM thruster [16], however this version of the GEM thruster was a two-stage thruster, with a separate non-gallium cathode. The work presented here is of the present incarnation of the GEM thruster, though an approximate and highly simplified ablation model has been used. Furthermore, the work here is different from previous studies as this GEM thruster utilizes a cathode that functions as both a mass injection surface as well as an electrode. This presented some difficulties in the mass flow characteristics as well as the setup of the magnetic field, as discussed later.

## 1.5 Motivation

In the past, experimental research has been performed on the GEM thruster [6-8]. This work involved measuring the arc impedance, exhaust velocities, and electron temperatures for a GEM thruster with a radius ratio (ratio of outer anode radius to inner cathode radius) of 3.4. Performance was predicted to improve by increasing the radius ratio to 5.

The work presented in this study incorporates the MACH2 code in replicating the results of the original experiment. Furthermore, performance is examined when the radius ratio is increased.

The layout of this thesis is as follows: Chapter 2 describes previous experimental results of the GEM thruster; Chapter 3 describes the MACH2 code; Chapter 4 describes the setup of the code inputs; Chapter 5 describes the results from the code; and Chapter 6 summarizes the conclusions of the study.

# Chapter 2 Description of Previous Testing

## 2.1 Introduction

The following gives a summary of the experimental data previously gathered at the University of Illinois Electric Propulsion Laboratory. This data was used for comparison with the simulation data from MACH2 (see Chapter 5 for the simulation results and comparisons).

## 2.2 Setup and Diagnostics

The GEM thruster itself utilized a coaxial geometry with a central gallium cathode configuration. The outer anode and insulator were composed of 316L stainless steel and boron nitride, respectively. The experimental results herein were performed at a radius ratio of 3.4. See Figure 2.1 below for images of the thruster and its dimensions.

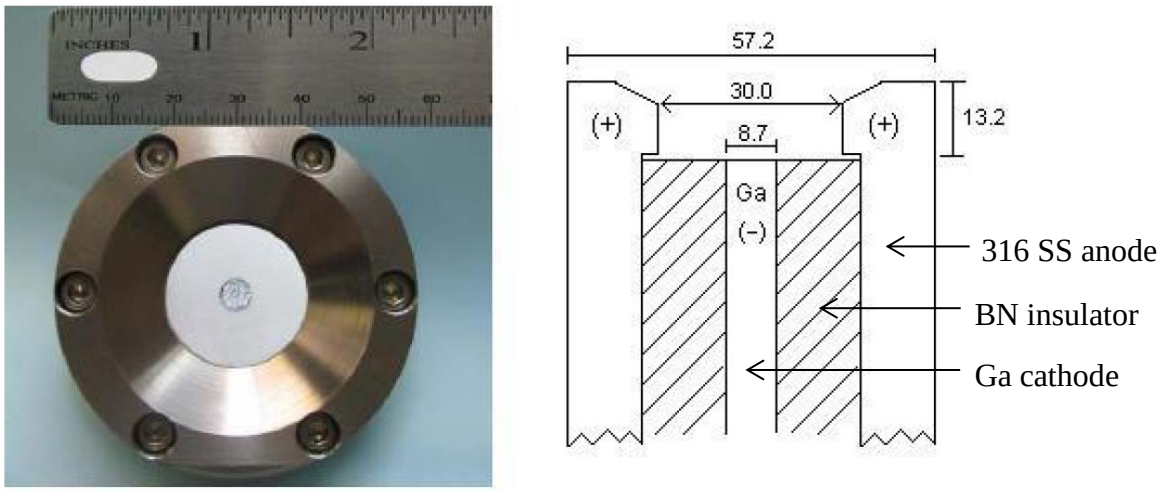


Figure 2.1: (a) Top view of thruster. (b) Cross sectional view (dimensions in mm) [6].

The experimental setup consisted of a vacuum chamber with a base pressure of 50 μTorr. For the setup of the electrical current, a 50 capacitor, five line pulse forming network (PFN) with a

maximum bank energy of 3.2 kJ was designed and used. The experimental discharge current pulse for this PFN is shown in Figure 2.2.

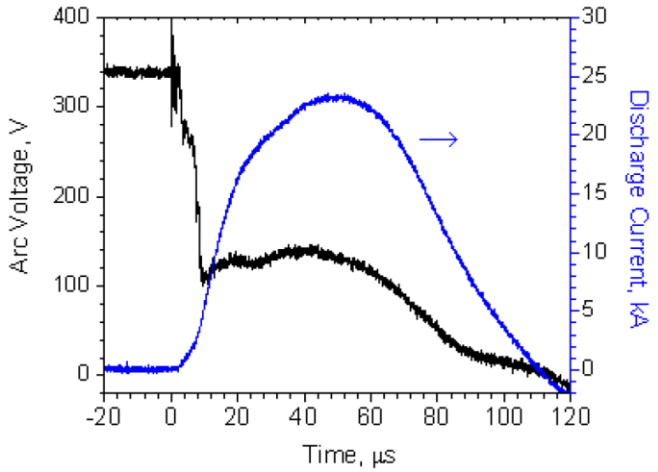


Figure 2.2: Experimental discharge current and arc voltage values vs. time [6].

Regarding the experimental data, several sets of data were measured and used in comparing with the MACH2 simulation. The discharge current was measured using a current-modeling transformer, and the arc voltage across the cathode and anode was measured with a high-voltage probe. Emission spectra data on the chemical species present were measured with a spectrometer. The mass flow rate was measured by weighing the gallium cathode before and after each test. Electron density and temperature data were measured with a triple Langmuir probe. Velocity measurements were obtained using crossed electrostatic probes and time of flight double probes. Magnetic field measurements were obtained using a magnetic field probe. Finally, thruster efficiency values were obtained.

### 2.3 Experimental Results

It should be noted that while experimental results for discharge currents of 7.3, 14.2, 17.8, and 22.6 kA were recorded, only results for 22.6 kA were used for comparison. Additionally as

mentioned above, a radius ratio of 3.4 was used, with a gallium cathode of radius 4.35 mm and a stainless steel anode of radius 15 mm.

### 2.3.1 Voltage, Emission Spectra, and Mass Flow Results

First, for the measured current of 22.6 kA, an arc voltage of 148 V was measured (see Figure 2.2). This experimental value was found to be within 10% of a calculated value of 139 V.

Emission spectra at different currents were obtained, which showed the presence of neutral, singly, and doubly ionized gallium molecules, as well as some iron from the anode. Additionally, triply ionized gallium ions were observed, with more Ga III spectra exhibited with higher current levels. In terms of the experimental mass flow rate, a rate of 6 g/s was measured.

### 2.3.2 Electron Density, Electron Temperature, and Velocity Results

For electron density, electron temperature, and velocity data, measurements were taken at locations past the exit plane of the thruster so as to show the axial and radial variation of the properties. These locations are shown below in Figure 2.3. The data at these locations were compared with the MACH2 data at the corresponding locations, with some exceptions: The experimental data at radial locations at 6 cm and ~8 cm were seen to be approximately equal to the data at ~4 cm and thus were neglected in the simulations so as to save computational time. Additionally, the axial location at 18 cm was similarly neglected, as keeping it would have increased computational time significantly.

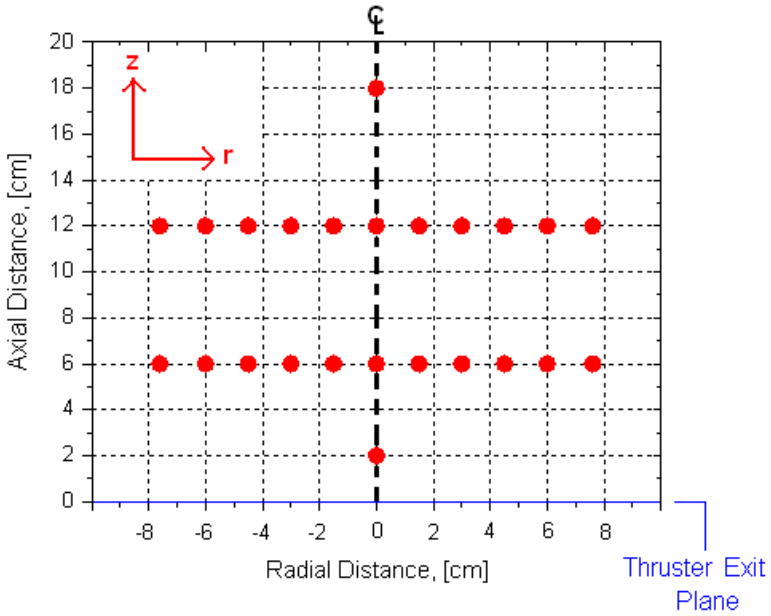


Figure 2.3: Location of experimental probes for electron density, electron temperature, and velocity measurements [6].

#### 2.3.2.1 Electron Density Measurements

The electron density (experimental uncertainty of ±40%) was measured to have a peak value of 2.2 x $10^{22}$ $m^{-3}$ at an axial distance of 2 cm from the exit plane of the thruster. The electron density was also shown to drop by approximately a factor of 10 at an axial distance of 18 cm from the exit plane. See Figure 2.4(a) for the electron density variation along the axis, and see Figure 2.4(b) for the radial variation.

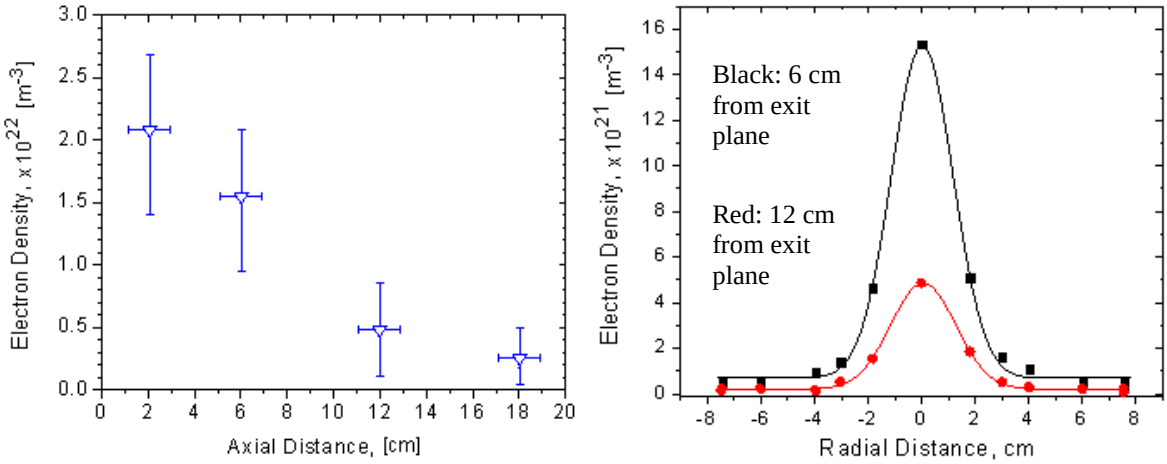


Figure 2.4: (a) Axial variation of electron density. (b) Radial variation of electron density [6].

### 2.3.2.2 Electron Temperature Measurements

The electron temperature (experimental uncertainty of ±15%) was found to be invariant with current, with a peak value of 3.6 eV at 2 cm from the exit. The electron temperature was also found to drop by approximately 40% at 2 cm in the radial direction and remain constant as r increased. See Figure 2.5(a) for the electron temperature variation along the axis, and see Figure 2.5(b) for the radial variation.

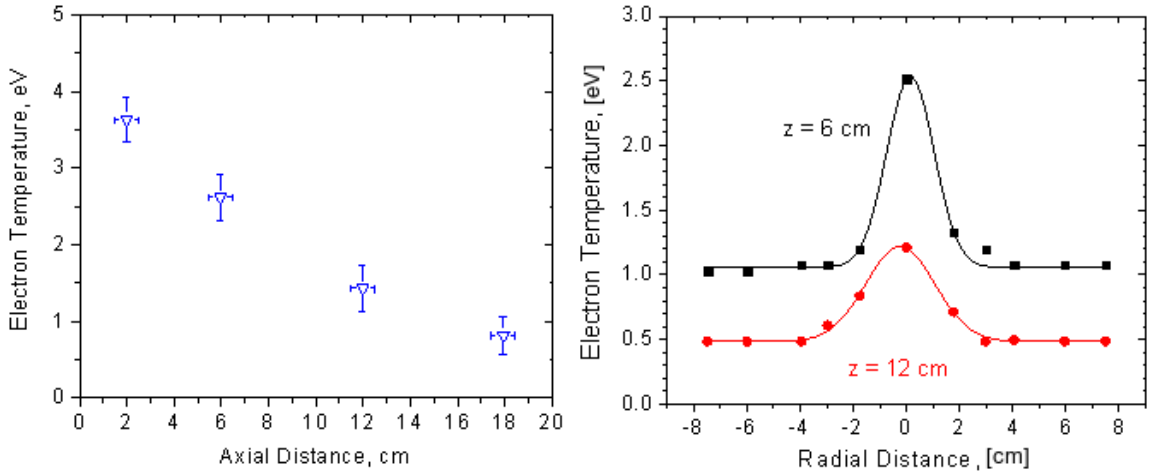


Figure 2.5: (a) Axial variation of electron temperature. (b) Radial variation of electron temperature [6].

### 2.3.2.3 Velocity Measurements

The velocity was measured with crossed probes (experimental uncertainty of ±40%) and floating double probes (experimental uncertainty of ±30%). See Figure 2.6(a) for the velocity variation along the axis for both methods, and see Figure 2.6(b) for the radial variation with the crossed probes.

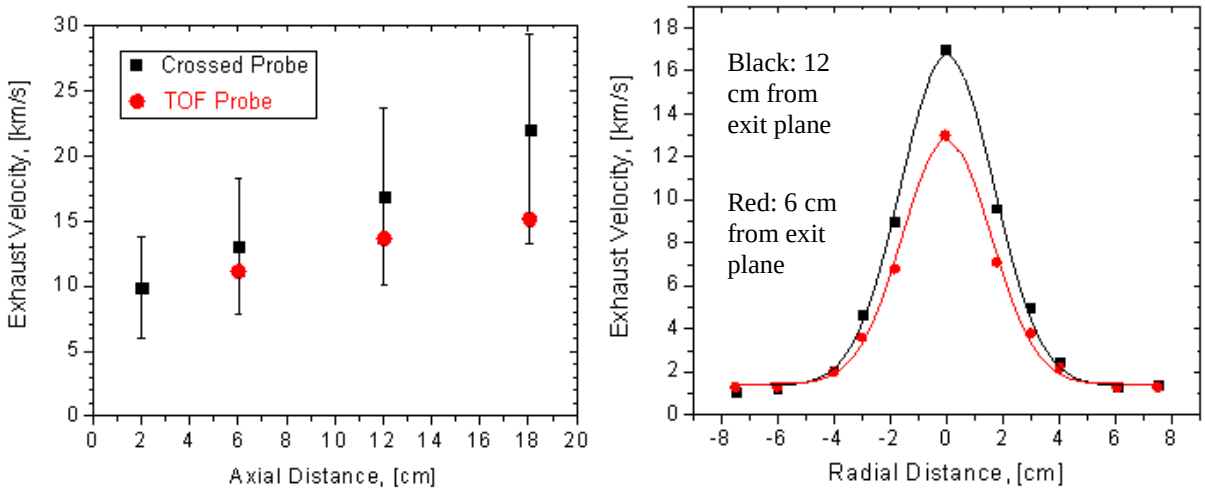


Figure 2.6: (a) Axial variation of velocity for crossed probes and floating double probes (TOF Probe). (b) Radial variation of velocity for crossed probes [6].

### 2.3.2.4 Magnetic Field Measurements

The magnetic field (experimental uncertainty of ±20%) was measured at locations of ±0, ±4.35, ±9.7, and ±15 mm from the axis along the cathode and insulator faces. See Figure 2.7 for the radial variation of the magnetic field.

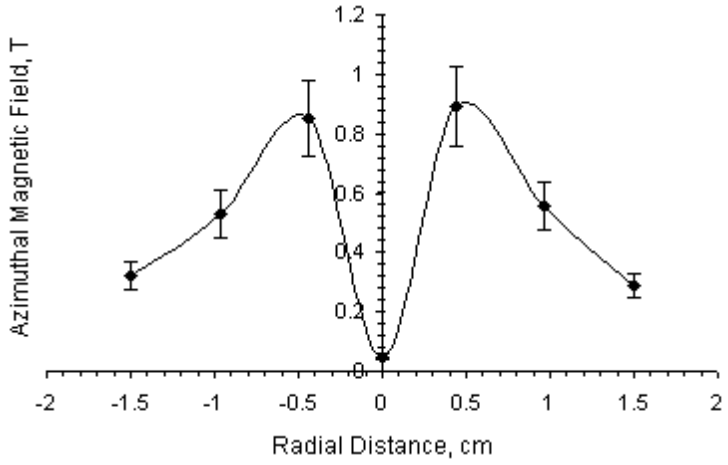

Figure 2.7: Radial variation of magnetic field [6].

### 2.3.3 Efficiency Calculations

Using experimental data, efficiency values were calculated for the radius ratio of 3.4, yielding an efficiency of 25%. Assuming electrical characteristics and mass bit values would stay the same for a radius ratio of 5, an efficiency of 30% was predicted.

# Chapter 3 Description of MACH2

## 3.1 MACH2 Description

As mentioned earlier, the simulation software used to replicate the experimental results was MACH2. MACH2, short for Multiblock Arbitrary Coordinate Hydromagnetic, is a code that can simulate various unsteady plasma setups and was developed in the mid-1980s as a U.S. Department of Defense code[17]. MACH2 creates simulations in two and a half dimensions – the half dimension functions as a third dimension, however it is referred to as a half dimension since the derivatives in that dimension are set to zero. A fully three dimensional version of the code exists (MACH3), however the code is not as mature as MACH2. For the purposes of this research, MACH2 was sufficient, as MACH2 can create simulations in either cylindrical or Cartesian orthonormal frames. In cylindrical coordinates, the radial and axial directions create the two dimensional plane, with the half dimension being the azimuthal direction that is assumed to be constant due to symmetry about the centerline axis [18]. (In the Cartesian frame, the x and y directions form the plane, with the z direction being the half dimension.)

MACH2 has various computational grid options. For example, it can run simulations in either Lagrangian or Eulerian frames, and the grid is able to change and adapt during the course of the simulation. (A description of all the grid options is outside the scope of this work, as only an Eulerian frame of reference was needed to create the simulation space consisting of the insides of the GEM thruster and the downstream region.) This computational grid is a mesh that is composed of "blocks," which consist of groups of cells. These blocks have four sides in the two dimensional plane, including sides that can be arcs. The cells are arranged inside these blocks and similarly have four sides in the two dimensional plane.

## 3.2 MACH2 Equations

There are several equations used to create simulations in MACH2, and they are listed here:

Mass continuity:

$$\frac{\partial \rho}{\partial t} = -\nabla \cdot (\rho \boldsymbol{u}) \tag{3.1}$$

Fluid momentum:

$$\rho \frac{\partial \boldsymbol{u}}{\partial t} = -\rho \boldsymbol{u} \cdot \nabla \boldsymbol{u} + \nabla \cdot (\gamma (P_e + P_i + Q) + \boldsymbol{M}) \tag{3.2}$$

Ion and neutral particle energy:

$$\rho \frac{\partial \varepsilon_i}{\partial t} = -\rho \boldsymbol{u} \cdot \nabla \varepsilon_i - P_i \nabla \cdot \boldsymbol{u} + \Phi_{ei} \tag{3.3}$$

Electron energy:

$$\rho \frac{\partial \varepsilon_e}{\partial t} = -\rho \boldsymbol{u} \cdot \nabla \varepsilon_e - P_e \nabla \cdot \boldsymbol{u} + \boldsymbol{J} \cdot \boldsymbol{E} - \Phi_{ei} \tag{3.4}$$

Faraday's law:

$$\frac{\partial \boldsymbol{B}}{\partial t} = -\nabla \times \boldsymbol{E} \tag{3.5}$$

Electric field:

$$\boldsymbol{E} = -\boldsymbol{u} \times \boldsymbol{B} \tag{3.6}$$

Current density:

$$\boldsymbol{J} = \frac{\nabla \times \boldsymbol{B}}{\mu_0} \tag{3.7}$$

Ideal gas equation of state:

$$P_{e(i)} = (\Gamma - 1)\rho\varepsilon_{e(i)} \tag{3.8}$$

In the equations above, ρ is the mass density of the fluid, **u** is the fluid velocity, $P_e$ is the electron pressure, $P_i$ is the ion pressure, Q is an artificial compressional viscosity pressure, γ is the Kronecker delta, **M** is the Maxwell stress tensor given by

$$M^{\alpha\beta} = \frac{1}{\mu_0}\left(B^{\alpha}B^{\beta} - \frac{1}{2}B^2\gamma^{\alpha\beta}\right) \tag{3.9}$$

**B** is the magnetic field, $\mu_0$ is the magnetic permeability constant, $\varepsilon_e$ is the electron internal energy, $\varepsilon_i$ is the ion internal energy, **J** is the current density vector, **E** is the electric field vector, $\Phi_{ei}$ is an electron ion coupling term, and Γ is the constant ratio of specific heats [18].

The general approach taken to setting up simulations in MACH2 is as follows:

a.) First, a coordinate system is chosen (cylindrical vs. planar), and the geometry of the model is input. This defines the two dimensional model grid using lines, arcs, and points.

b.) Top-level physics parameters pertinent to the problem are turned on or off. Additionally, parameters governing numerical methods are defined (i.e., various time step options).

c.) Material properties are input.

d.) The blocks, which represent regions of materials and/or properties, are given initial conditions.

e.) The boundary conditions along the sides of the blocks (the sides in the two dimensional model plane) are defined.

f.) Output parameters are set. These configure the format of the resulting files, i.e., whether they are Tecplot data files and what variable information (velocity values, magnetic field values, etc.) they contain.

Assuming no problems exist in the input file, the MACH2 code is then run.

# Chapter 4 Simulation Setup

## 4.1 Hardware

The computational resources for this project included an Intel Core i7-2630QM at 2.0 GHz laptop and two dual core desktops. It should be noted that MACH2 does not allow for parallel processing. Due to the computational time required, the processor temperatures on the laptop would sometimes reach 85°C when running four different instances of MACH2, and consequently the laptop needed to be kept cool (usually being placed on an external fan and put under an air conditioner). This setup was alleviated by using the dedicated desktops for long duration computation.

## 4.2 Software

Running MACH2 requires Linux, and for this study, Ubuntu (versions 11.04 and 11.10) was selected. For analyzing the data and plots, the flow visualization software Tecplot 360 was used.

## 4.3 Model Setup

MACH2 groups inputs into several categories: parameters dealing with top-level physics and top-level computational processes; parameters that are used in setting up the physical geometry of the model; parameters that define the material properties of the medium; parameters that control initial and boundary conditions; parameters that set up a current waveform; and parameters that define the output of the code. The relevant choices of input parameters of these groups are described below:

### 4.3.1 Top-Level Physics and Computational Processes Setup

Problem end time: The end time was chosen such that steady state could be achieved, which was observed when no visible changes occurred over time in contour plots of various flow properties, such as density, temperature, and velocity. For the results described later, an end time of 50 μs was chosen. The real-time hours spent on these computations depended on the size and complexity of the model; for the 50 μs results, the simulations took several days to complete.

Time step: In general, the choice of time step is important as it affects how a code runs: having it too large can reduce accuracy and possibly cause the code to stop running; having it too small can needlessly increase the computation time. In MACH2, there are different time steps for several of the various processes, with the overall time step for a cycle being chosen as the smallest of these individual time steps. Additionally, the user specifies an initial time step and a maximum time step. For this study, it was found that the code encountered errors and stopped running depending on the choice of the maximum time step, however setting the maximum time step to $10^{-10}$ seconds resulted in stable code execution.

Geometry choice: As mentioned in the MACH2 description above, MACH2 can solve problems in either planar or cylindrical geometry. For this study, cylindrical geometry was selected, with the axis of symmetry going through the center of the cathode.

Equation of state: MACH2 allows for the equation of state to be obtained by two different ways: analytic models or data tables. Since tabular data on gallium are not provided, the ideal gas analytical model was used, which required specifying the atomic weight, the ratio of specific heats, and an average ionization state. These are discussed later in the material properties setup section.

Electron and ion temperatures: MACH2 controls whether the ion and electron temperatures are equal. If the electrons and ions are assumed to be in equilibrium, the temperatures are set equal to each other. This was not assumed in this study.

Hydrodynamics setup: There are several possible computational options relating to the hydrodynamics equations. These were mostly kept to their default values.

Radiation model: MACH2 allows for radiation models, however these were not used in this study.

Thermal diffusion model: Thermal diffusion was turned on, and the corresponding computational options were mostly kept to their default options.

Magnetic field setup: The thermal source term in Ohm's law was not included in the computations. Initially this was left on, but it seemed to be negatively affecting the magnetic field as predicted by Ampere's Law. Also, the magnetic field was set to consist only of the azimuthal (theta) magnetic field component.

Magnetic diffusion: Magnetic diffusion was turned on, and the corresponding computational options were mostly kept to their default options.

Multigrid algorithm: MACH2 utilizes a memory algorithm called multigrid, which takes the grid of cells and examines coarser versions of the grids (i.e., with proportionally fewer cells). In this study, multigrid was turned on, as turning it off resulted in incorrect thermal and magnetic diffusion.

Hall effect: There are two ways of adding the Hall effect to the simulation, however there were problems implementing it, and since the Hall parameter was predicted to be relatively low, it was turned off.

### 4.3.2 Physical Geometry Setup

The following is a brief description of creating a model in MACH2. First, one specifies whether cylindrical or rectangular coordinates will be used. For this study, cylindrical coordinates were used, which meant creating a cross-section view of the r-z plane of the GEM thruster. It should be noted that in MACH2, when cylindrical coordinates are used, the plots are still generated looking like x-y plots, however the x axis on the plot now represents the r axis, the y axis represents the z axis (cylindrical axial coordinate), and the z axis (out-of-plane rectangular component) represents the theta axis.

With this setup now in mind, the user then creates quadrilateral "blocks" in the r-z plane by specifying (r,z) coordinates. Note that these blocks are not computational cells themselves; instead they contain the cells. Initial conditions can then be set inside the blocks themselves, and boundary conditions can then be set on the boundaries of these blocks. The GEM thruster was modeled from the dimensions given in Figure 2.1b, with the simulated radius of the anode varying depending on which radius ratio was being examined. To compare the experimental measurements with the simulation, the flow region past the exit of the thruster was also put into the model space. A diagram of the model is shown below in Figure 4.1. The block numbers are arbitrary: blocks 1, 2, 3, and 4 represent the region inside the thruster, with blocks 1 and 3 representing the region above the cathode and blocks 2 and 4 representing the region above the insulator. Blocks 5, 6, 7, 10, 11, and 12 represent the region outside the thruster, and a

separation between the three blocks 5, 6, and 7 and the three blocks 10, 11, and 12 exists only for convenience. Blocks 8 and 9 represent part of the region in the cathode and insulator, respectively, and they only exist to set up the magnetic field correctly. This is discussed later in the circuit model setup in Section 4.3.4.

Note also that the model in Figure 4.1 shows a radius ratio of 3.4, however a radius ratio of 5 was also examined. This required only changing the value of the r coordinate values along the anode radius and changing the number of cells to maintain uniform cell spacing.

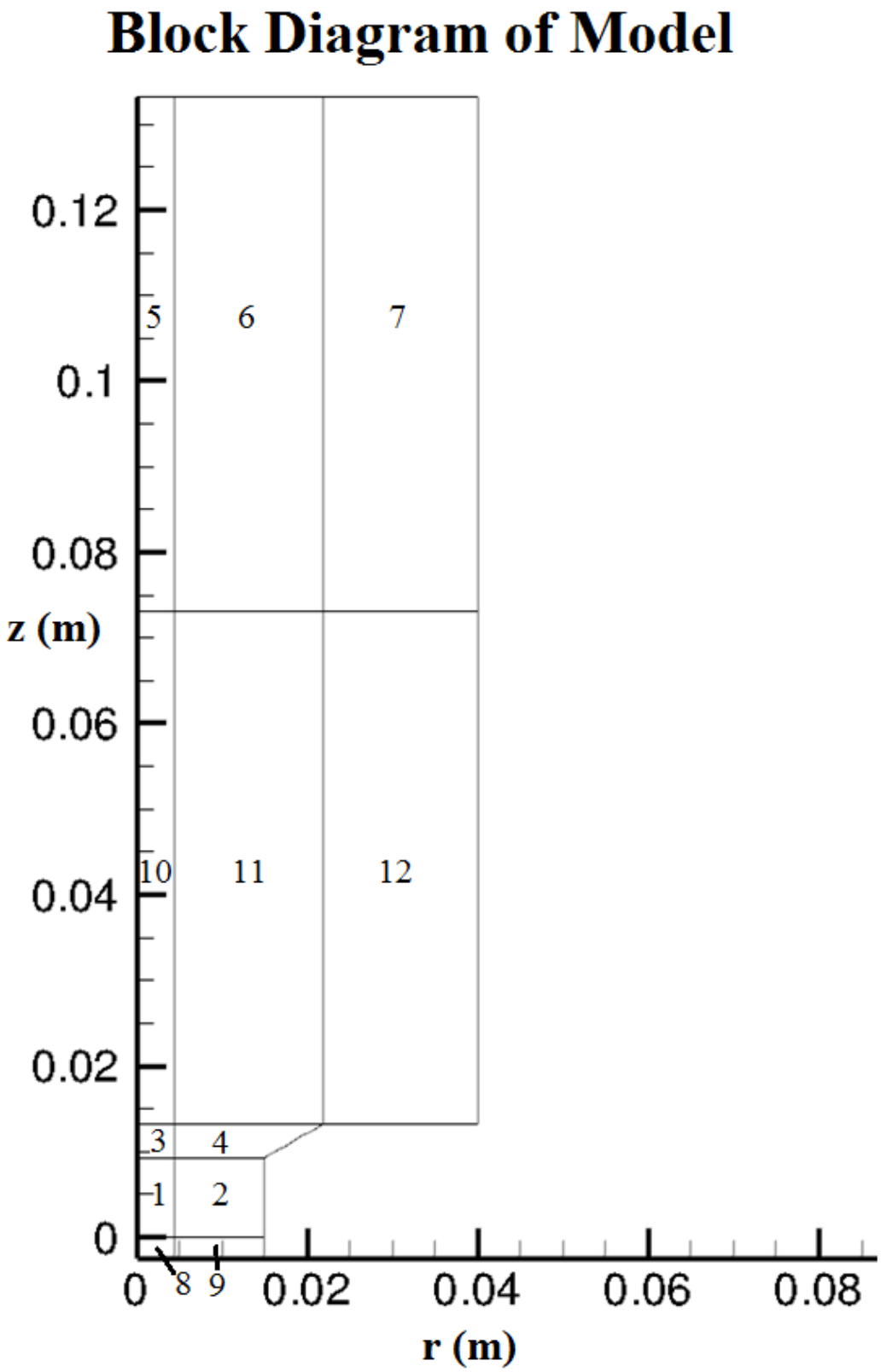


Figure 4.1: Model setup (radius ratio of 3.4) with block numbers shown. The location of z = 0 marks the cathode and insulator faces.

### 4.3.3 Material Property Setup

In MACH2, a number of different materials can be specified with corresponding properties. These materials are then set as initial conditions for the blocks. A summary of the material properties is as follows:

Atomic weight: The atomic weight of gallium, 69.72 g/mol, was used.

Average ionization state: As described in Section 2.3.1, an ionization state of between 2 and 3 was observed for the 22.6 kA current. Based off the spectroscopic data, it was believed to be closer to 2. In this study, an ionization state of 2 was chosen.

Ratio of specific heats: The ratio of specific heats for a monatomic gas is 5/3. Since gallium is monatomic, this value was used.

Density floor values: In MACH2, there are various parameters to set maximum and minimum limits on certain parameters, such as density and temperature. For this study, there were three values of floor density that were of interest: absolute floor density, floor density for hydrodynamics, and floor density for joule heating. The absolute floor density controls the absolute minimum density that occurs in the simulation – densities are equal to this value or greater. The floor density for hydrodynamics controls the minimum density at which the hydrodynamic equations (mass conservation, momentum conservation, etc.) are used – wherever the density is lower than this floor value, that region is unaffected by the hydrodynamic equations. The floor density for joule heating operates similarly – it controls the minimum density at which joule heating is performed. Any location where the density is lower than this floor value, joule heating is not performed.

As described earlier, in theory, by increasing the radius ratio of an MPD thruster, the thrust should increase. For early MACH2 results, this was not found to be the case – the thrust was seen to remain approximately constant for different radius ratio values. Upon further inspection, it was determined that the material density close to the anode radius was smaller than the set hydrodynamic floor density (not having this parameter set led to the code running into errors and stopping). Consequently, the momentum of this region was not being affected by the magnetic field. To fix this, the absolute floor density was set such that it was slightly higher than the hydrodynamic floor density. This guaranteed that regions with the lowest density in the simulation would still be affected by the hydrodynamic equations. The order of magnitude for these values was determined by trial: higher orders of magnitude resulted in mass flow values that had more than 10% variance along the axis, whereas the mass flow should be approximately constant; lower orders of magnitude resulted in other errors, such as temperatures that were too high. The joule heating floor density was found similarly through trial. These floor density values chosen are summarized below in Table 4.1.

Table 4.1: Floor density values.

| | |
|---|---|
| Absolute | $5.05 \times 10^{-6}$ kg/m$^3$ |
| Hydrodynamic | $5 \times 10^{-6}$ kg/m$^3$ |
| Joule heating | $5 \times 10^{-3}$ kg/m$^3$ |

Resistivity model: The resistivity model computed a Spitzer plasma resistivity, which relates the resistivity (the inverse of the conductivity) to the electron temperature $T_e$ as $T_e^{-3/2}$. A constant resistivity model was tried, however the Spitzer resistivity yielded the most reasonable voltage measurements, and the simulation value of the conductivity better matched its corresponding experimental value (this is discussed in Section 5.7).

Ionization model: There are four types of ionization models in MACH2: a constant mean ionization model, a mean ionization model linear between two set temperatures, a mean ionization state model using the Saha equation for hydrogen, and a mean ionization state model using collisional equilibrium for atomic hydrogen. Implementing a Saha equation for gallium was discussed early in the project, however this would have entailed changing code, which was outside the scope of this work. Consequently, a constant mean ionization model was used, with an ionization state of Z = 2 being used, as mentioned earlier.

Thermal conductivity model: While a Spitzer model for the thermal conductivity exists in MACH2, because thermal conduction is not an important part of GEM thruster physics, it was assumed that a constant thermal conductivity model would be sufficient for this study, for which a value of $10^4$ J/(m-s-eV) was used.

### 4.3.4 Initial Conditions and Boundary Conditions Setup

Material selection: Material properties (as defined in MACH2) were kept the same throughout the modeling space, except for the region representing the physical cathode and insulator, which had floor densities for joule heating and hydrodynamics that were of a sufficient order of magnitude such that joule heating and hydrodynamics would not occur in the corresponding blocks. This behavior was desired because these blocks were only meant to set up the magnetic field.

Cell numbers: Inside each block a set amount of cells was specified. Spacing (cell number per length) was kept fairly regular throughout the blocks in the axial and radial directions. The number of cells was also picked such that high resolution data were obtained. Additionally, the multigrid algorithm described above has certain requirements on cell numbers (i.e., best results

occur with even numbers of cells). See Figure 4.2 below for the cells in the radius ratio of 3.4 case.

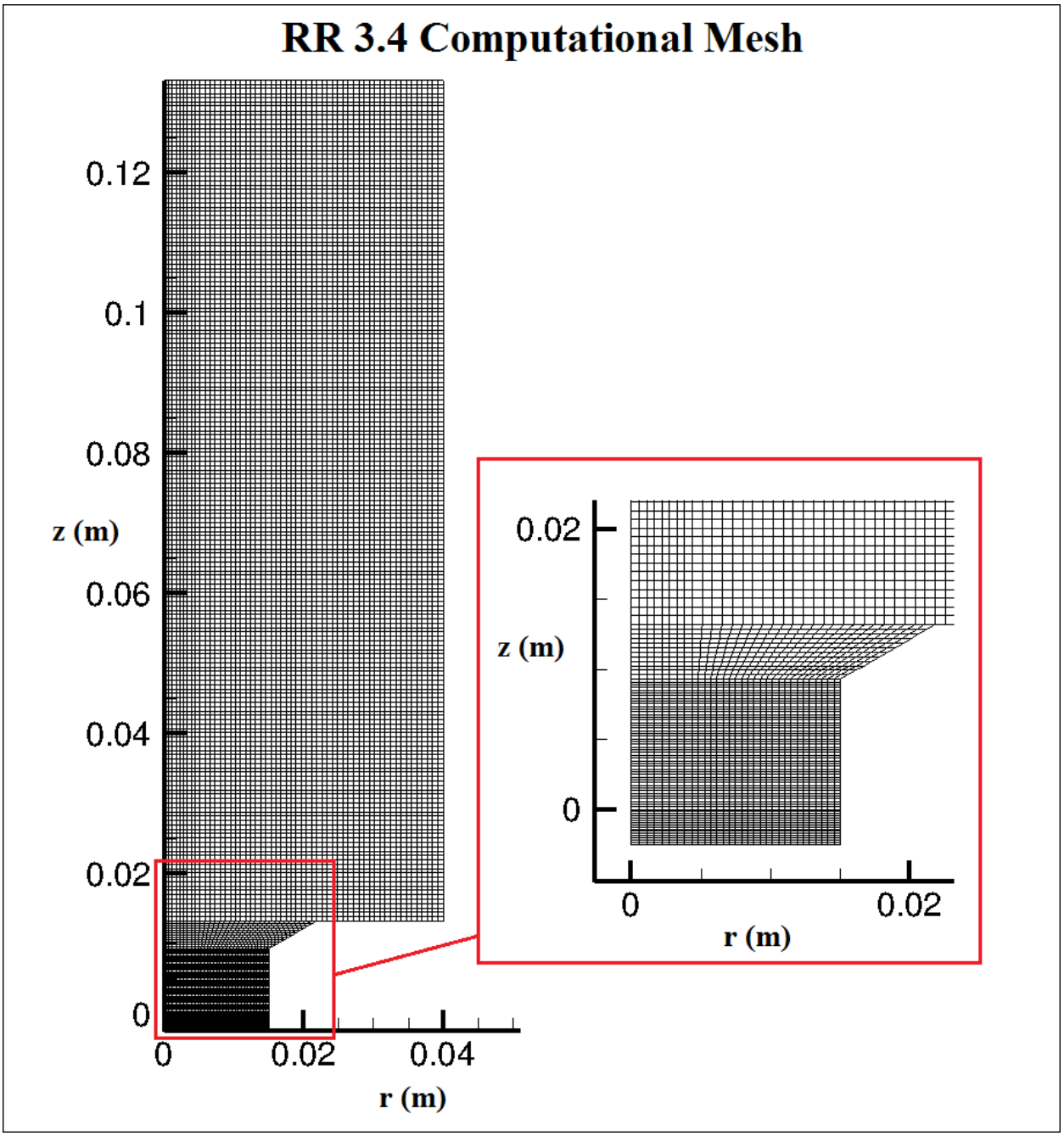


Figure 4.2: Model setup for radius ratio of 3.4 with cells shown.

Initial conditions: There were two initial conditions set: initial temperature and initial density. The initial temperature throughout the model was set to room temperature (290 K), and the initial density was set to a number slightly higher than the floor density so as to replicate vacuum conditions.

Before going into detail about the boundary conditions, a brief explanation of boundary condition notation is needed. In MACH2, a numbered block has four corners and four sides, each of which an index is given. These indices are useful for describing locations of boundary conditions, as each unique boundary can then be given as (side number, block number) or (corner number, block number). Please see Figure 4.3 below for an example block with the sides numbered.

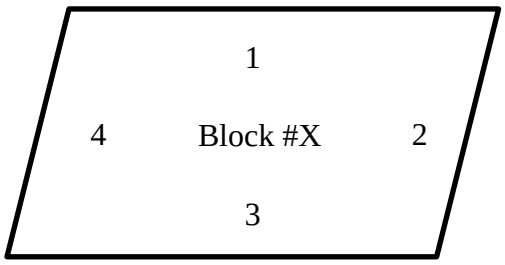


Figure 4.3: Boundary numbering convention for blocks. (Note: Blocks are not necessarily rectangular – they are defined to have four sides and four corners.)

Axis conditions: Along the axis of symmetry (boundary 4 of blocks 1, 3, 5, 8, and 10), several boundary conditions had to be made showing that boundary as the axis of symmetry. This included prohibiting mass flow across the axis boundary, setting the azimuthal magnetic field component equal to zero along the axis, and disallowing thermal conduction across the axis.

Open conditions: Along the "open" regions (boundary 1 of blocks 5, 6, and 7; and boundary 2 of blocks 7 and 12), several boundary conditions had to be made relating to the fact that these

boundaries were not constrained by a wall surface. This included allowing mass flow across these boundaries. Additionally, boundary conditions were implemented that set the azimuthal magnetic field component to zero along these boundaries. This was done to force no current from traveling from these boundaries to the cathode. A similar boundary condition was also placed at the top of stainless steel portion of the thruster (boundary 3 of block 12). This was to force the current to flow out from boundary 2 of blocks 2 and 4.

Cathode face conditions: At the cathode face (boundary 3 of block 1), mass flow conditions were implemented. These included specifying a density and velocity at which the gallium ablated. Additionally, as blocks 8 and 9 were created only to set up the magnetic field correctly (see below under "Magnetic Field BCs"), a thermal insulator boundary condition had to be implemented as well so as to insulate block 8 from the flow region. Additionally, a material boundary condition had to be specified so that the mass flow material was correct.

One major difficulty with the cathode boundary was that the velocity and density input values did not match the output mass flow – for example, setting an axial velocity BC of 385 m/s and a density BC of 0.2 $kg/m^3$ resulted in a velocity of approximately 2 km/s and a density of approximately 0.055 $kg/m^3$ directly next to the cathode. It was then decided to use the input conditions as "knobs," meaning that while desired output values would not match the input values, relations could be made between the input and output values such that one could plug in the desired output values and then determine what values would need to be input.

Additionally, MACH2 allows for setting a boundary temperature, however setting an input mass flow temperature (originally set at the approximate gallium boiling temperature) did not seem to have an effect – the output temperature near the cathode stayed mostly constant. It was believed

this occurred due to the boundary being over specified – having the density, velocity, and temperature specified along with potentially including the joule heating effects and/or the resistivity calculation was causing a problem. It was concluded that the temperature would remain unspecified, as the temperature inside the thruster was shown to be several eV in the simulations, which was not unreasonable given experimental data of the electron temperature being 3.6 eV at 2 cm from the exit of the thruster.

Another difficulty encountered was that the material ejected at the cathode face did not expand fully out to the anode radius. Having the material expand out to the anode radius is necessary to observe the effects of increasing the radius ratio. With this lack of expansion, there were negligible increases in thrust for increased radius ratio. It is unknown why this happened, although there are two theories: One is that in a numerical sense, the floor density values described above somehow limited the material from expanding out to the anode radius. However, changing the floor density values did not seem to fix this issue. The second theory is a more physical explanation: In gas-fed MPD thrusters, the gas propellant is fed through the region between the cathode and the anode. Theoretically for large radius ratios, gas propellant would be present in the entire region between the cathode and the anode. In the GEM thruster however, the propellant is the gallium, which is ablated from the cathode. Theoretically for large radius ratios, the ablated gallium would still originate from the cathode, however there would be an anode radius at which the ablated gallium would not expand completely radially, and any increases to the radius ratio would not result in increased performance. For this study, it was assumed that the issue was due to a numerical issue as described above, so to fix this, a second mass flow condition was implemented on the insulator face to account for the lack of expansion. The total mass flow (6 g/s) was still achieved, however a portion of that (~0.8 g/s) was set to

flow from the insulator. This amount of ~0.8 g/s was used as it was the smallest amount that allowed for a noticeable amount of material to reach the anode. The effect of the insulator mass flow was determined by first running the simulations without the insulator mass flow conditions, and then running them with the insulator mass flow conditions.

Insulator face conditions: As described above, two cases were run: that with the insulator face having a mass flow BC and that with the insulator face having no mass flow BC, so as to measure the effect of the additional mass flow. For the case of having the mass flow BCs on, the BCs on the insulator face (boundary 3 of block 2) matched those on the cathode face boundary, with exception of different input density and velocity values. Similarly, these BCs were treated as knobs rather than the actual output values, and they were adjusted accordingly to achieve a significant amount of material near the anode. For the case of having the mass flow BCs off, the BCs on the insulator face included prohibiting mass flow across the axis boundary and disallowing thermal conduction across the axis.

Finally, it needs to be mentioned that on internal boundaries (those not on the exterior of the model space), it is necessary to have the same BCs on either side of the boundary. Thus, the same BCs mentioned above were also placed on the adjoining boundaries of adjacent blocks.

Magnetic field BCs: In theory, within a wire, the azimuthal magnetic field varies linearly with the radius, and outside the wire, it varies inversely with the radius. Near the cathode face of the GEM thruster, the azimuthal magnetic field had to show these correlations. Setting up the BCs to reflect this behavior in MACH2 requires a pair of BCs to mark at what boundary the magnetic field ceases varying linearly with radius and begins inversely varying with radius. At first, these BCs were set up in the flow field, however this resulted in the code not working. To circumvent

this issue, blocks 8 and 9 were created that represented the physical cathode and insulator, insofar that only the magnetic field is simulated but not any other properties are simulated, i.e., the density of the solid materials. The aforementioned pair of BCs was thus set on boundary 2 of block 8 and boundary 4 of block 9. This setup was deemed to work, as the azimuthal magnetic field in the flow field near the cathode had the correct behavior.

### 4.3.5 Current Waveform Setup

MACH2 has different ways of setting up a circuit; one of which allows the specification of various current values at certain times. This method was at first used to replicate the current-time plot from Figure 2.2, however this was changed in favor of reaching a steady state value of the maximum current quickly. Specifically, the rise time from going from 0 kA to 22.6 kA was set at 0.1 μs, at which point the simulation continued at 22.6 kA until the end time was reached.

### 4.3.6 Output Setup

MACH2 allows various properties to be output from the simulation. In this study, at intervals of 0.05 μs, a variety of variables such as density, electron temperature, and pressure were output into Tecplot format.

# Chapter 5 Model Results

## 5.1 Introduction

This section is split into several parts: voltage measurements and comparisons; electron density measurements and comparisons; magnetic field results and comparisons; pressure simulation results; temperature results and comparisons; conductivity results and comparisons; velocity results and comparisons; and finally an analysis of the mass flow rate and momentum flow rate.

## 5.2 Voltage

### 5.2.1 Method Used for Calculating Voltage

Before discussing the voltages calculated in the simulations, a brief explanation on the method used to calculate the voltage is needed. Voltage is defined by the line integral

$$V = -\int_C \boldsymbol{E} \cdot \boldsymbol{dl} \tag{5.1}$$

where C is a path and **E** is the electric field along a distance **dl** on C. In calculating the voltage in these simulations, the voltage was seen to vary somewhat on the path taken. Initially, an average voltage was defined using the path from r = $r_a$ and z = 4.635 mm travelling radially inward to r = 3.262 mm and z = 4.635 mm, then travelling axially toward the cathode to r = 3.262 mm and z = 0 mm. The value z = 4.635 mm corresponds to the halfway point between the cathode/insulator face and the edge of the anode, and the value r = 3.262 mm bisects the cathode into two regions of equal area. This setup allowed for relatively simple calculations, as only purely radial or purely axial components of **E** were examined. In addition, a second option was

examined in which the voltage was defined using the axial electric field along the axial path from z = 0 to z = 13.3 cm, effectively measuring from the cathode face to infinity.

### 5.2.2 Voltage Values for Radius Ratios 3.4 and 5

Using the above methods, the voltages were computed and compared. The first method yielded voltage values of 194 V and 310 V for the radius ratios of 3.4 and 5, respectively, with the majority of the difference between the two values coming from the radial path. While some increase in the radial component of **E** was expected for the increased radius ratio, these results showed a significant increase in voltage. In examining the corresponding voltage values for the cases of no mass insulator mass flow, it was also observed that the voltages measured without the insulator mass flow condition were lower than those with the insulator mass flow condition. To avoid this increase from the insulator mass flow, the second above method (involving only axial integration) was used, in which voltage values of 148 V and 222 V were measured for the radius ratios of 3.4 and 5, respectively. See Figure 5.1 below for the axial electric field as a function of z for both radius ratios.

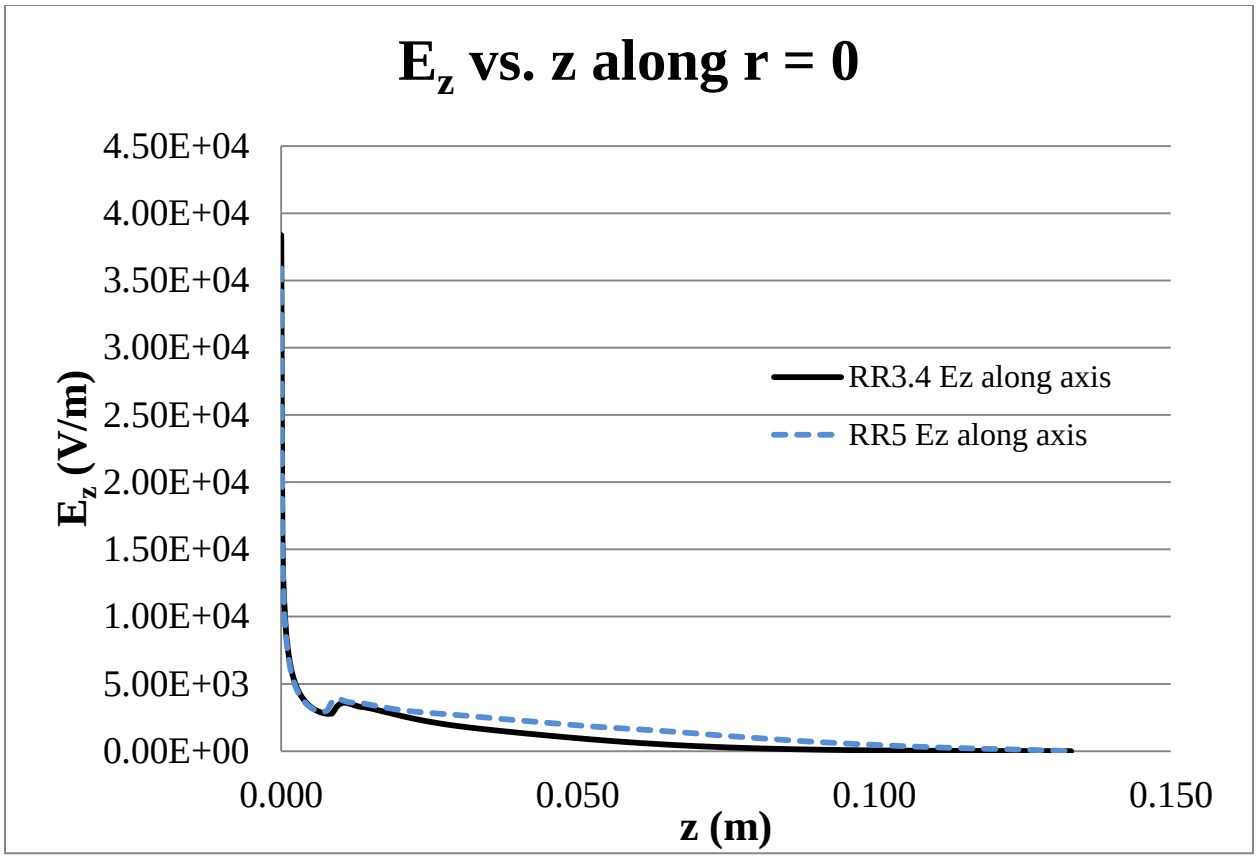

Figure 5.1: Axial electric field vs. z for both radius ratios.

Experimentally, a voltage of 148 V was measured for the radius ratio 3.4. The experimental value included the effects of electrode sheaths, which were estimated as 1.5 times the 6.0 eV ionization potential of gallium on each electrode, totaling 18 V. Therefore an adjusted experimental value of 130 V was used in comparison with the MACH2 data, yielding a 14% error.

### 5.3 Electron Density Comparisons for Radius Ratio of 3.4

Figures 5.2 and 5.3 below show the electron density as a function of axial and radial directions, respectively. The axial measurements were taken along r = 0 along the z axis from the face of the cathode to 12 cm from the exit plane of the thruster (z = 13.3 cm). The axial simulated value matched very well the experimental measurement at 2 cm from the exit of the thruster (z = 3.3

cm), however after z = 3.3 cm the density dropped to being approximately half an order of magnitude too low compared to the experimental values. Similarly, the radial distribution showed simulated values lower than the experimental values, even accounting for the ±40% experimental error.

There were possibly two reasons for the simulated values being lower than the experimental values. First, as mentioned earlier, a constant ionization state of 2 was chosen for these simulations, however experimentally there were some Ga III particles observed for the 22.6 kA current. Changing the ionization state to a higher value would increase the electron density in the simulation. However, the downstream axial values would likely still be too low. A more likely possibility is that even though the mass flow was kept approximately constant to 6 g/s throughout, the simulation velocities were, on average, higher than experimental values. Thus, the simulation's lower electron density values might have been connected to the higher velocity values. This might indicate that the source of the disagreement stems from a term(s) in MACH2's momentum equation.

Finally, Figure 5.4 below shows a contour plot of the electron density. Note that there were some electrons in the corner where the anode meets the insulator. This was due to the forced insulator mass flow boundary condition, as described earlier.

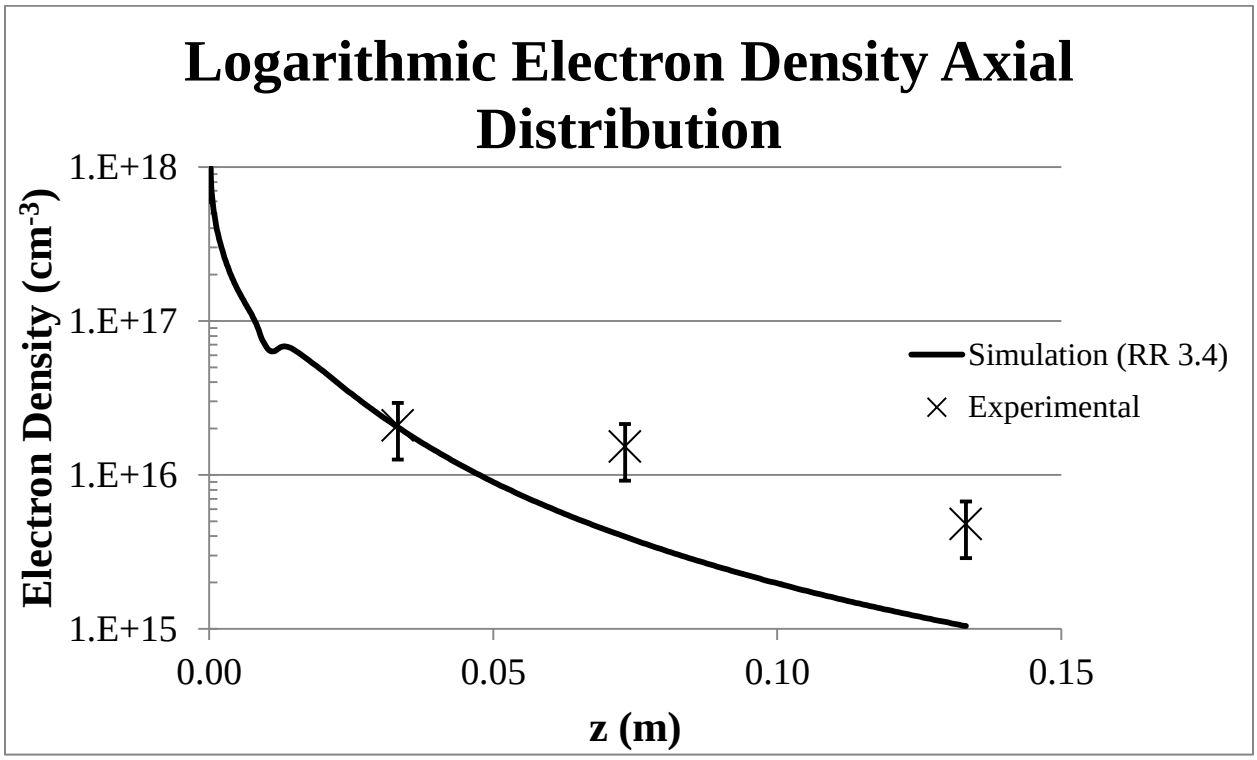


Figure 5.2: Axial variation of electron density for simulation and experimental (±40%) values.

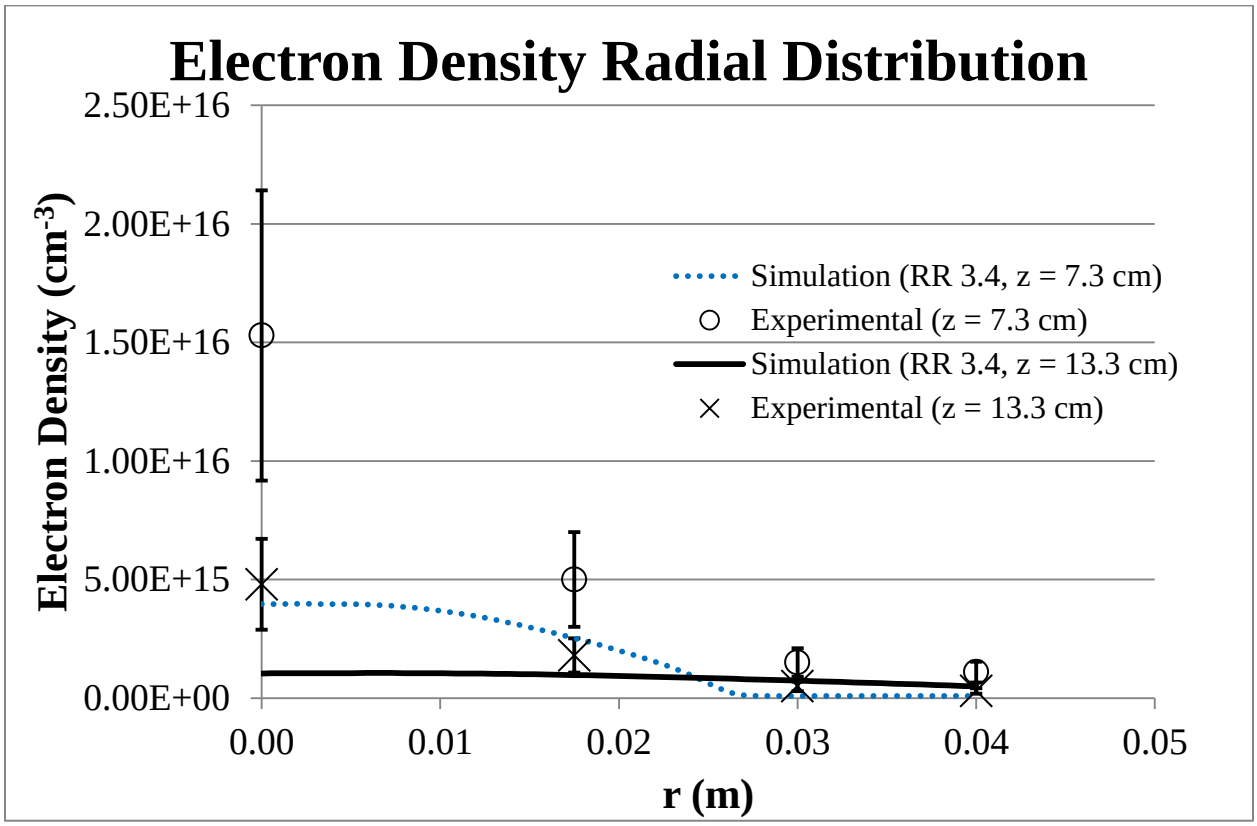


Figure 5.3: Radial variation of electron density for simulation and experimental (±40%) values.

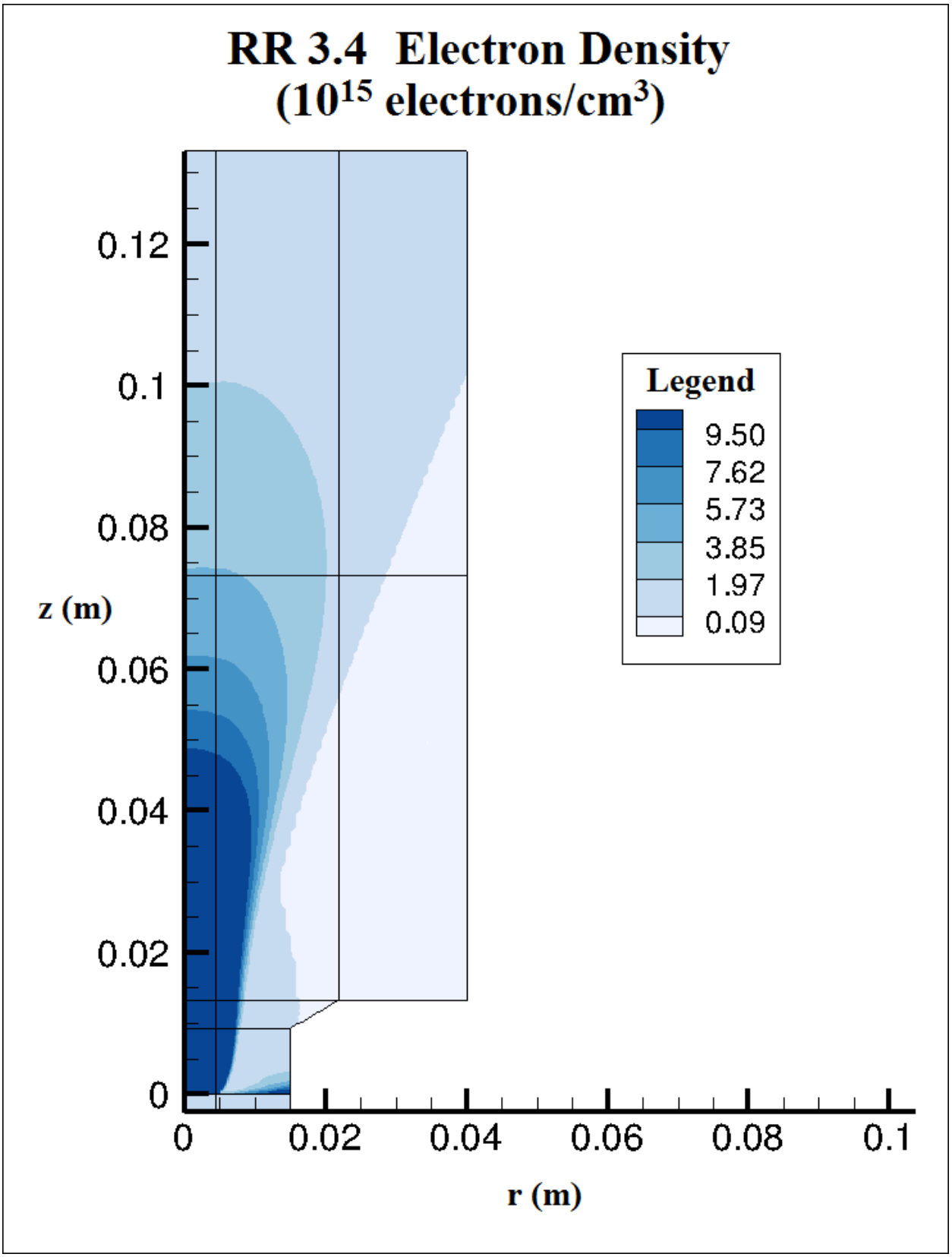


Figure 5.4: Electron density contour plot for radius ratio of 3.4.

## 5.4 Magnetic Field

Figure 5.5 below shows a comparison of the azimuthal (theta direction) magnetic field for simulated, experimental, and theoretical values. The experimental values were taken at the face of the cathode and the insulator, and the simulated values were taken one cell away in the axial direction from the face (at approximately 0.2 mm). Because the current flowing through the cathode was analogous to the current flowing through a wire, the theoretical magnetic field values corresponded to the magnetic field in a wire, which is given by:

$$B_\theta = \begin{cases} \dfrac{\mu_0 I}{2\pi r_c^2} r & \text{for } r \leq r_c \\ \dfrac{\mu_0 I}{2\pi r} & \text{for } r \geq r_c \end{cases} \tag{5.2}$$

The simulated, experimental, and theoretical data all corresponded very well. The simulation showed a linear dependence on r from r = 0 to r = $r_c$, implying a constant axial current density at the cathode, and it also showed an inverse dependence on r from r = $r_c$ to r = $r_a$. Additionally, it showed maximum and minimum values that corresponded well with experimental data.

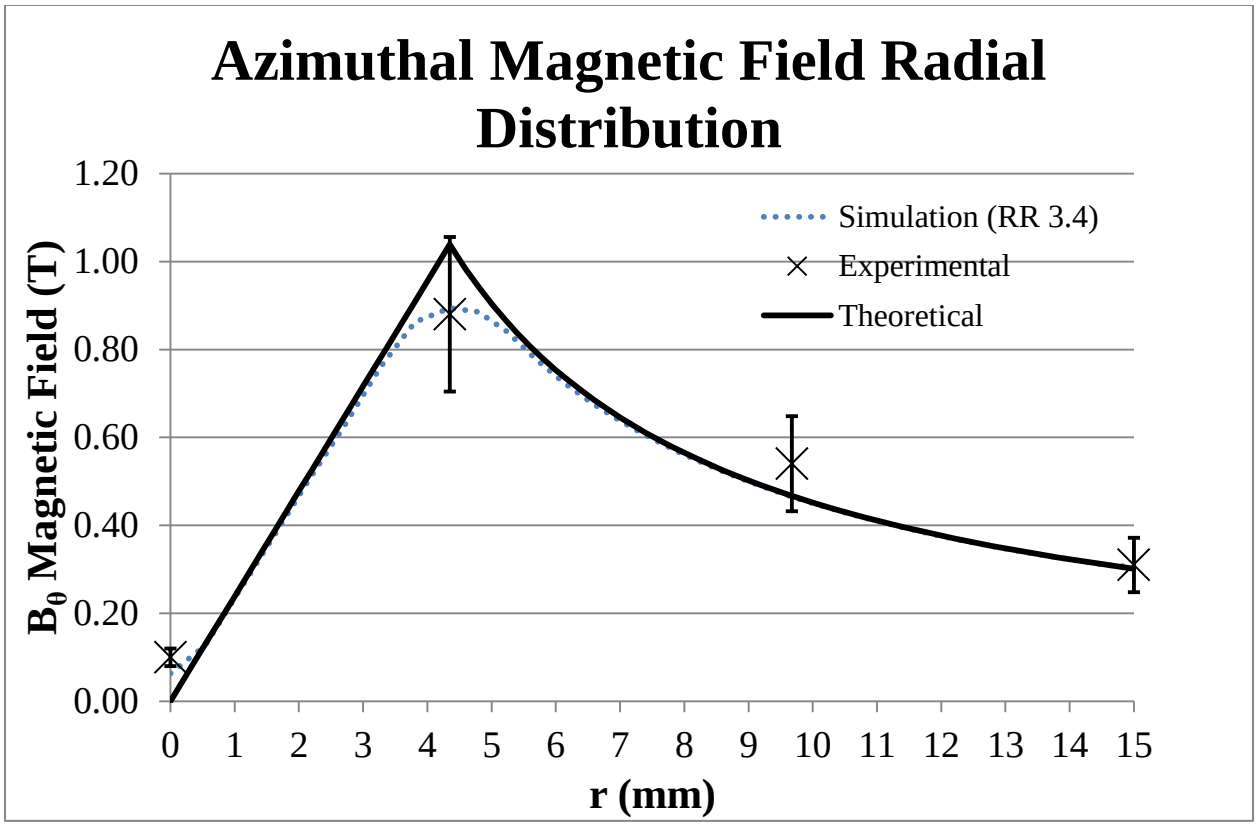


Figure 5.5: Radial variation of magnetic field at cathode and insulator face for simulation, experimental (±20%), and theoretical values.

Figure 5.6 below shows the magnitude of the azimuthal magnetic field as it extends downstream. Again, note that the region $z < 0$ corresponds to the physical cathode and insulator and hence did not contribute to the overall hydrodynamics of the simulation.

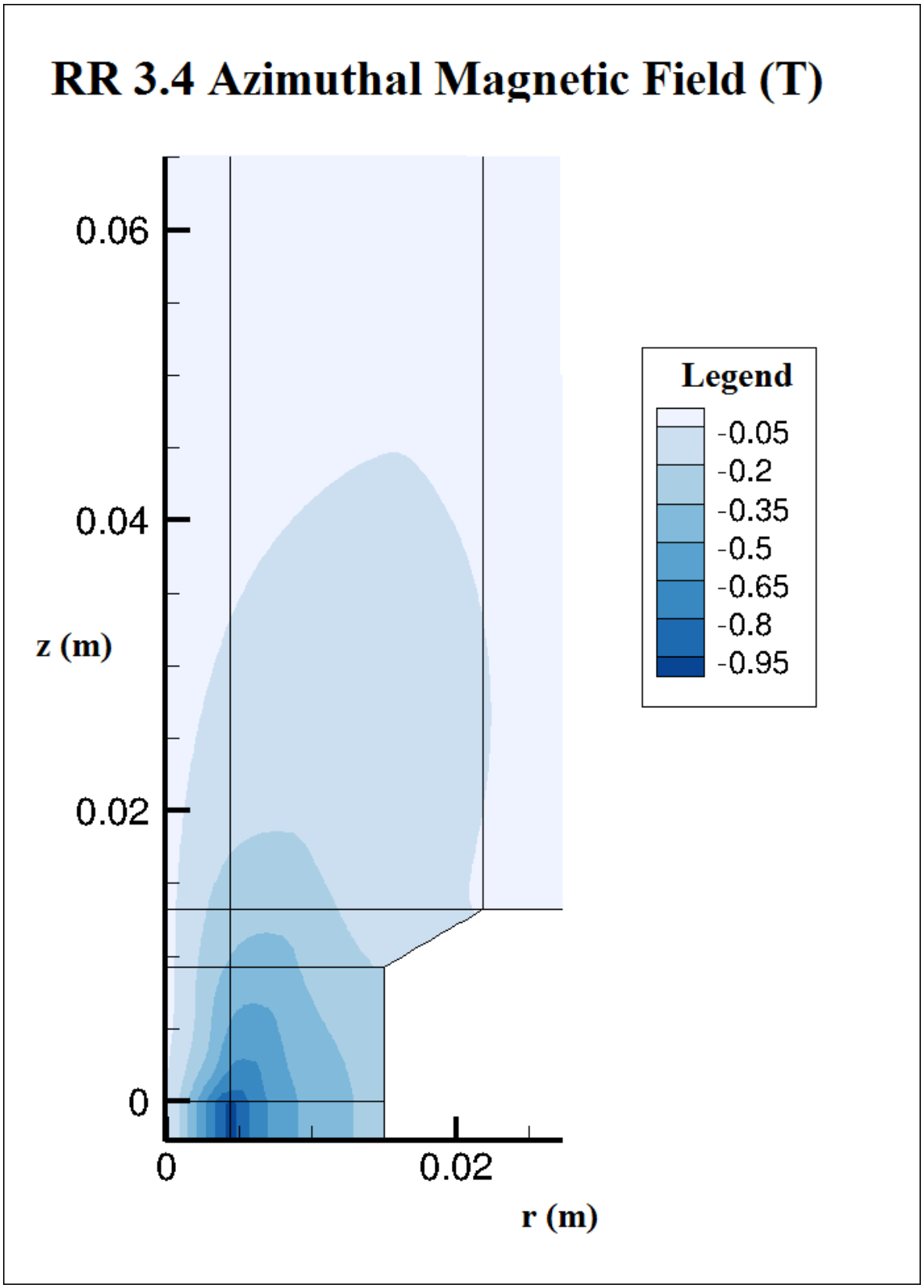


Figure 5.6: Magnetic field (azimuthal component) contour plot for radius ratio of 3.4.

### 5.5 Pressure for Radius Ratios of 3.4 and 5

The pressure, equal to the gas pressure plus the magnetic pressure, was examined for both radius ratios. A plot of pressure along the length of the axis and magnetic pressure along the cathode radius ($r_c$) is shown below in Figure 5.7. Along the axis, the smaller radius ratio had a higher pressure up until the divergence of the anode (z = 9.3 mm), and past that point, the larger radius ratio had a higher pressure. This higher pressure might have been due to the larger radius ratio having a higher pinch effect due to the larger radially inward **j** x **B** force. Along $r_c$, the magnetic pressure was approximately equal for both radius ratios. It should also be noted that the pressure closer to the cathode might not have been accurate due to the difficulty in setting the mass flow boundary conditions.

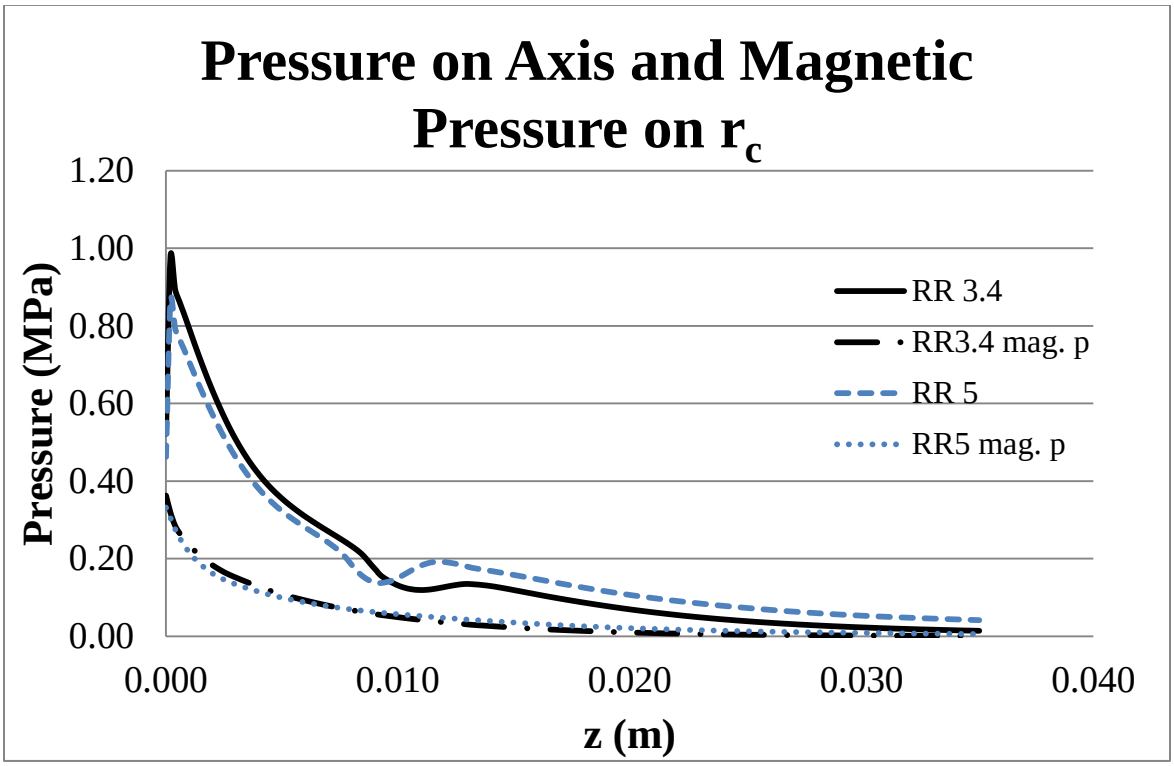


Figure 5.7: Pressure along axis and magnetic pressure along $r_c$ for both radius ratios.

Contour plots for the pressure are shown below in Figures 5.8 through 5.11. Figures 5.8 and 5.10 show the pressure contours for the radius ratios of 3.4 and 5, respectively. (Note that the pressures in the cathode and insulator regions were non-zero since the magnetic field induced a magnetic pressure there.) Figures 5.9 and 5.11 show the pressure contours near the cathode for the same radius ratios. The behavior is shown to resemble that stated above: for the smaller radius ratio, the pressure was higher closer to the cathode but lower further downstream. This is in contrast to the larger radius ratio having a lower pressure closer to the cathode but a higher pressure downstream. Again, this was likely due to the larger magnetic pinch effect.

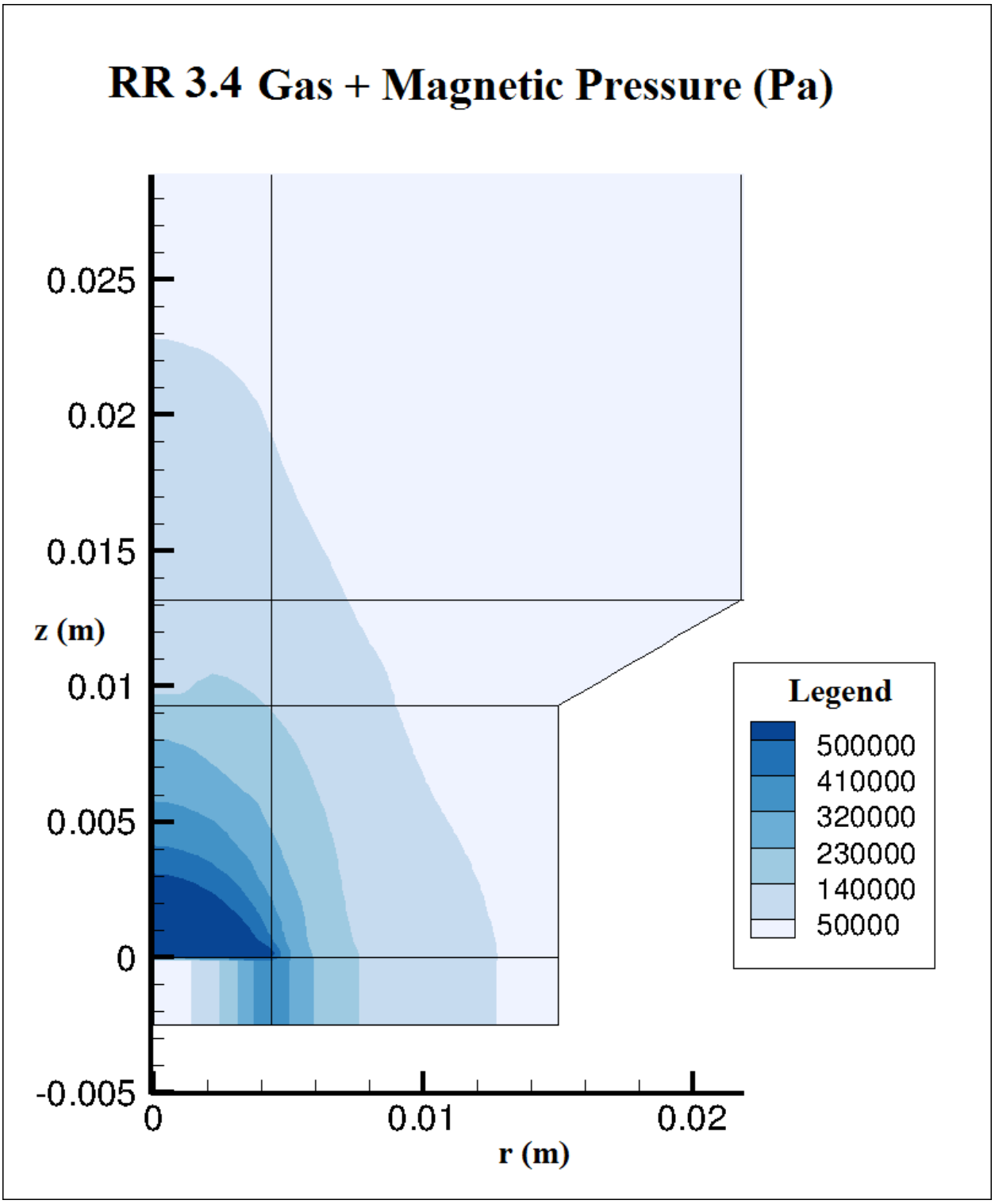


Figure 5.8: Pressure contour plot for radius ratio of 3.4.

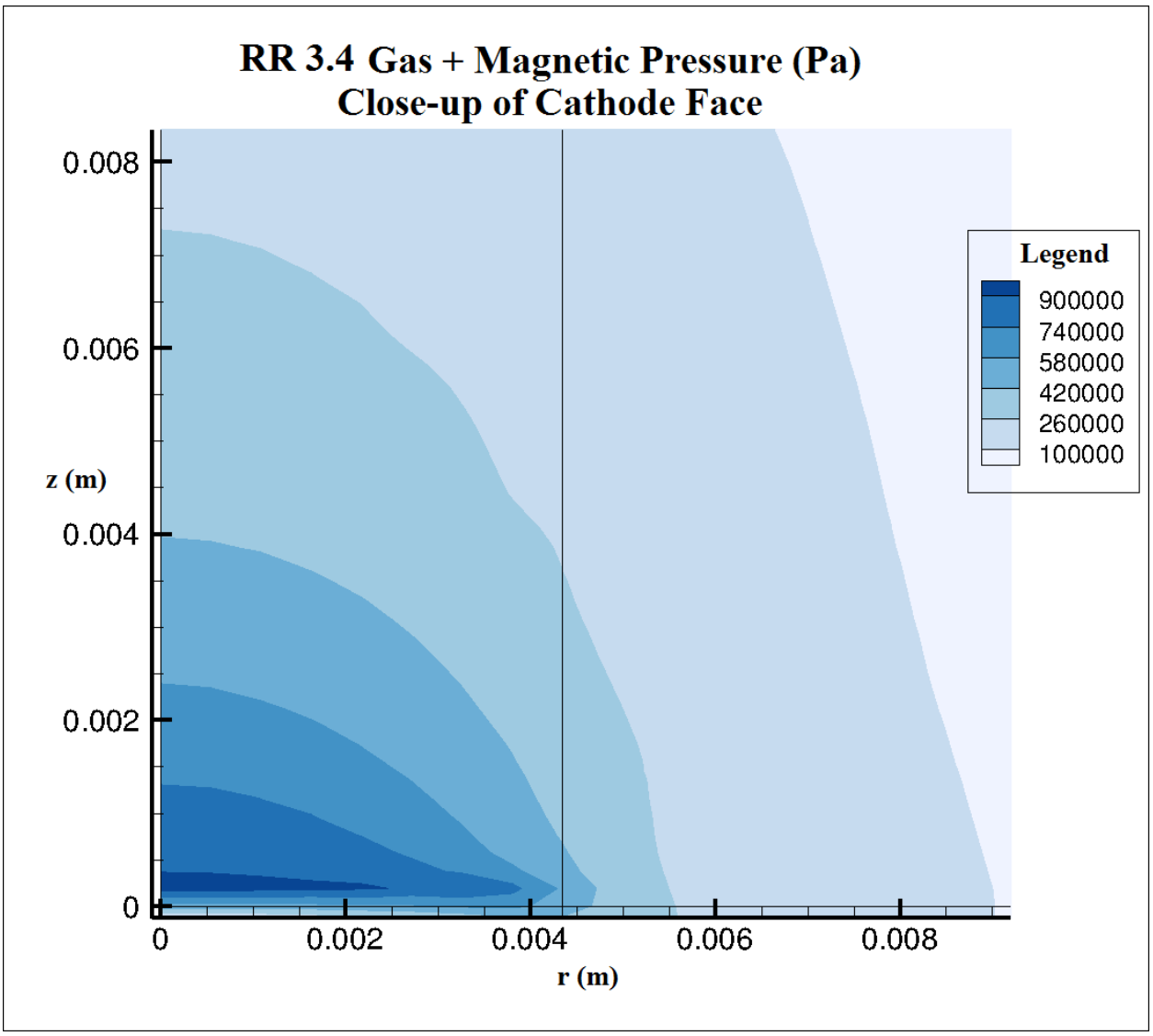


Figure 5.9: Pressure contour plot for radius ratio of 3.4 – cathode face region.

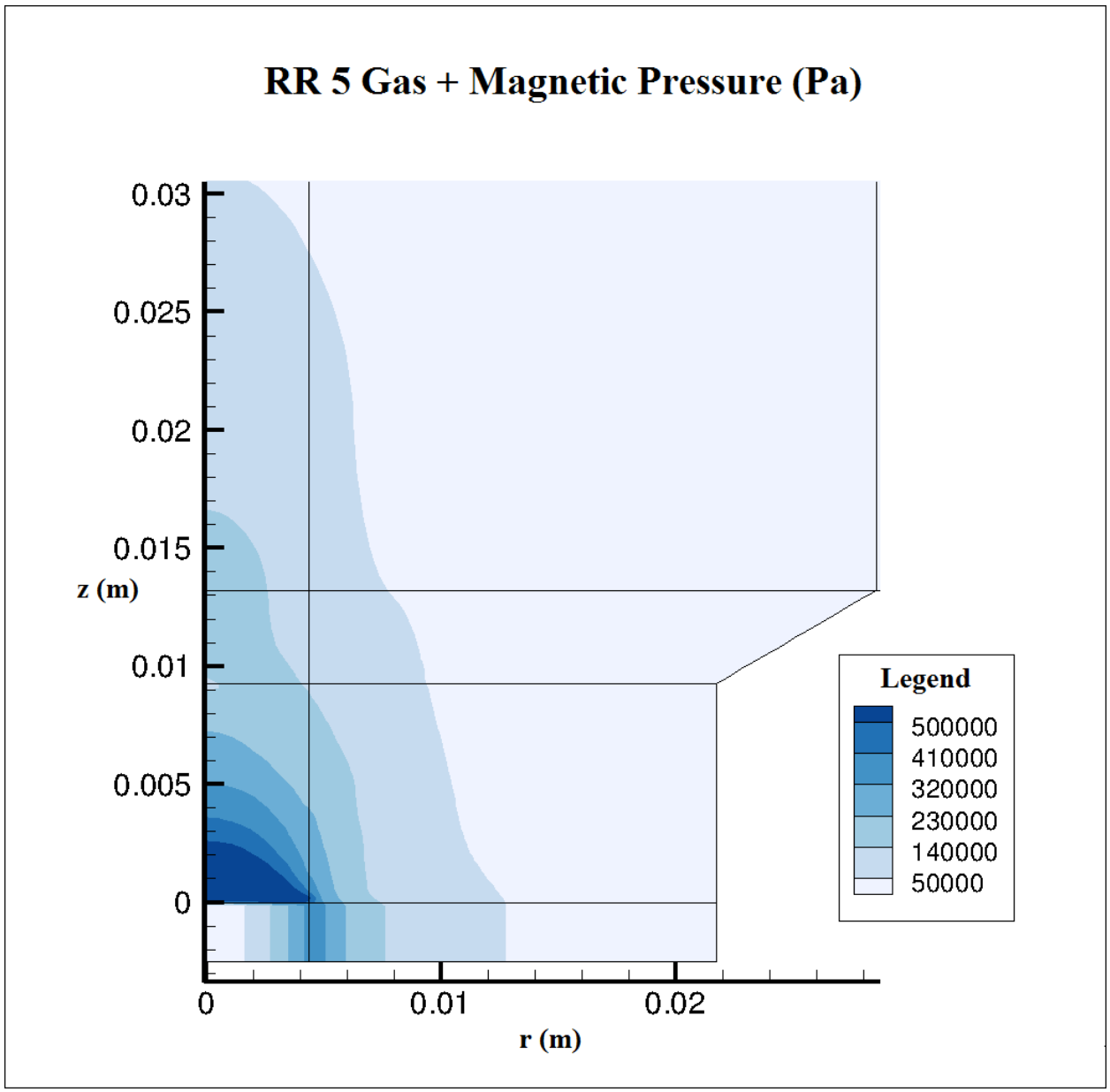


Figure 5.10: Pressure contour plot for radius ratio of 5.

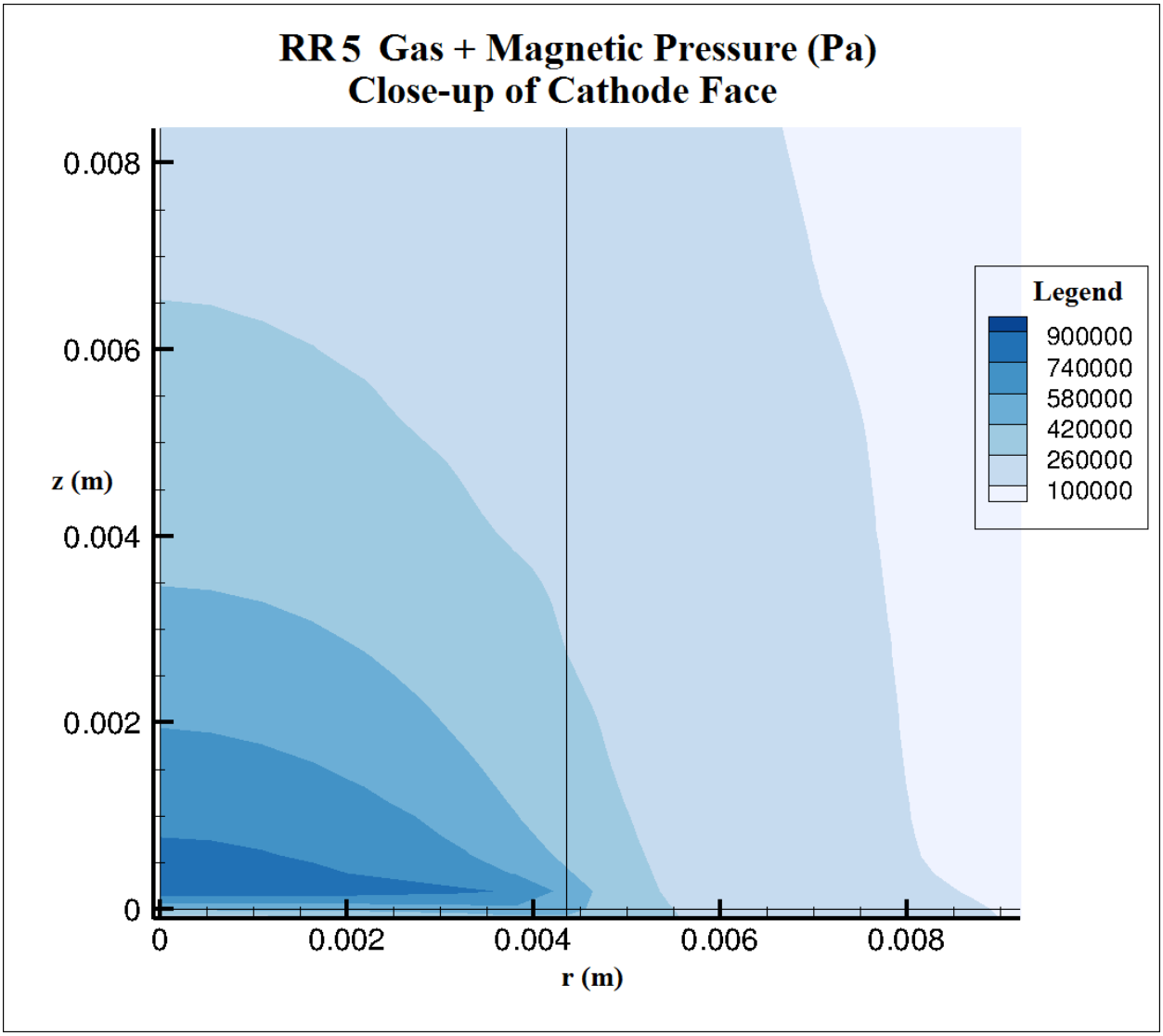


Figure 5.11: Pressure contour plot for radius ratio of 5 – cathode face region.

The pressure along the face of the cathode and insulator (at approximately z = 0.2 mm) was also plotted as a function of radius and is shown below in Figure 5.12 for both radius ratios. These profiles were roughly parabolic, and like the results above showing the smaller radius ratio having a larger pressure inside the thruster, here the smaller radius ratio had a higher pressure along the radial direction.

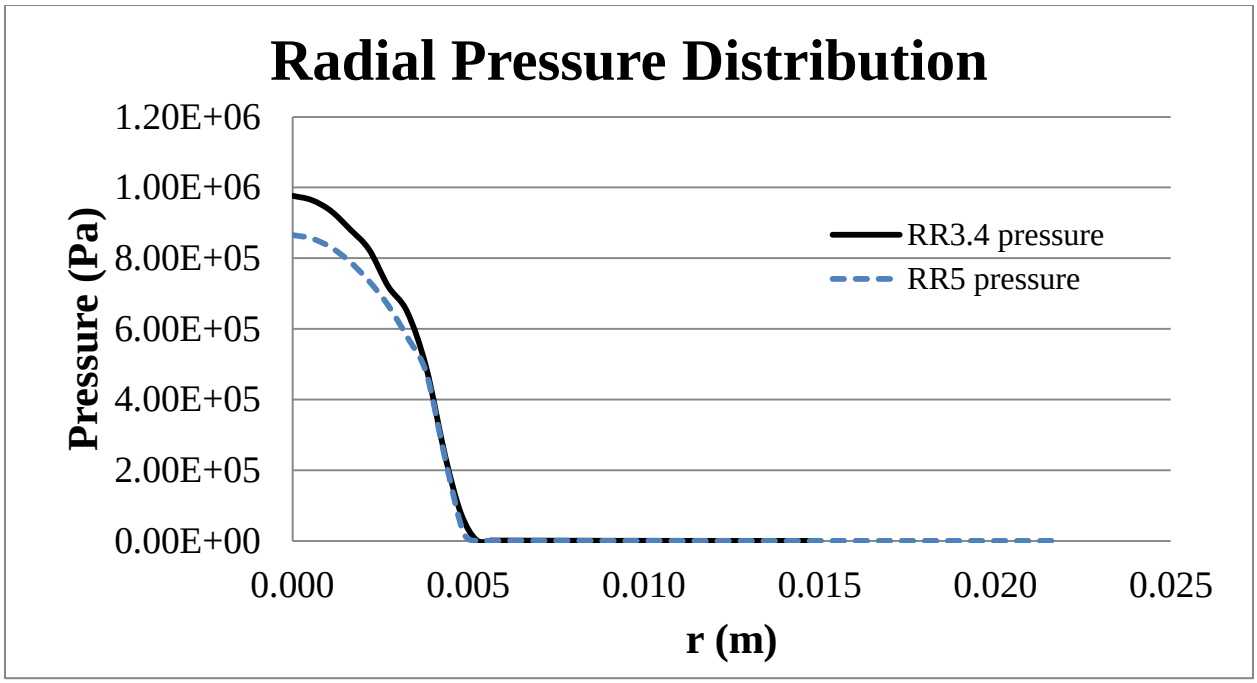


Figure 5.12: Radial pressure distribution at cathode/insulator face.

The radial pressure distribution was then used to calculate the force acting on the faces of the cathode and insulator. This was done by integrating the pressure over the area of the cathode/insulator faces for both radius ratios. The resulting cathode and insulator forces for the two radius ratios were shown to be fairly close, and these results are seen below in Table 5.1.

Table 5.1: Forces from integrating pressure.

| | RR 3.4 | RR 5 |
|---|---|---|
| Force on cathode (N) | 38.7 | 35.4 |
| Force on insulator (N) | 2.8 | 2.5 |

The predicted force due to **j** x **B** effects along the cathode face is given by

$$F_{z,cathode} = \frac{\mu_0 I^2 C}{4\pi} \tag{5.3}$$

where $\mu_0$ is the vacuum permeability [$4*\pi*10^{-7}$ (V-s)/(A-m)], I is the current, and C is a constant relating to the geometry of the cathode (for this study C = 0.5, which corresponds to a flat

cathode surface). Here $F_{z,cathode}$ = 25.5 N. Since the simulations showed higher force values on the cathode face, this shows the potential presence of an electrothermal thrust component.

### 5.6 Electron and Ion Temperature Comparisons for Radius Ratios of 3.4 and 5

Figures 5.13 and 5.14 below show the electron temperature for the radius ratio of 3.4 as a function of axial and radial directions, respectively. The axial measurements were taken at r = 0 along the z axis from the face of the cathode to 12 cm from the exit plane of the thruster (z = 13.3 cm). The peak temperature was shown to be approximately 10 eV inside the thruster near the exit plane. It should be noted that while the melting temperature of gallium is approximately 0.2 eV, the temperature near the cathode face was much higher. While joule heating might have resulted in some heating of the plasma, this high temperature at the cathode was likely due to the difficulty involved in setting the boundary conditions at the cathode face, as described in Section 4.3.4.

The axial temperature at z = 3.3 cm was shown to be very close to the experimental value. For axial measurements further downstream as well as the radial measurements, the MACH2 values were lower than what was experimentally measured. For the axial measurements, the overall behavior of temperature decreasing downstream was observed in both sets of data. For the radial measurements at these downstream locations, the simulated temperatures were approximately constant across the plane perpendicular to the axial direction. This is in contrast to experimental radial measurements, which showed a peak at the centerline, followed by an approximate constant temperature in the radial direction.

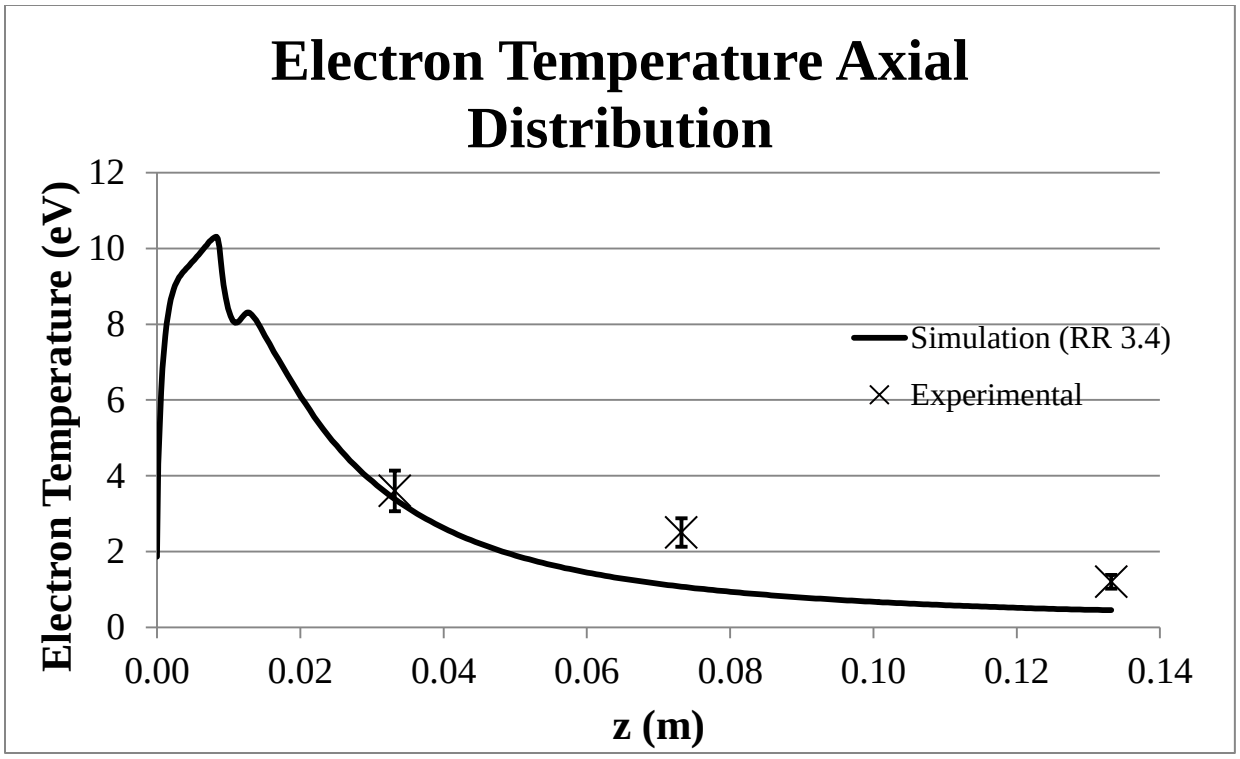


Figure 5.13: Axial variation of electron temperature for simulation (RR = 3.4) and experimental (±15%) values.

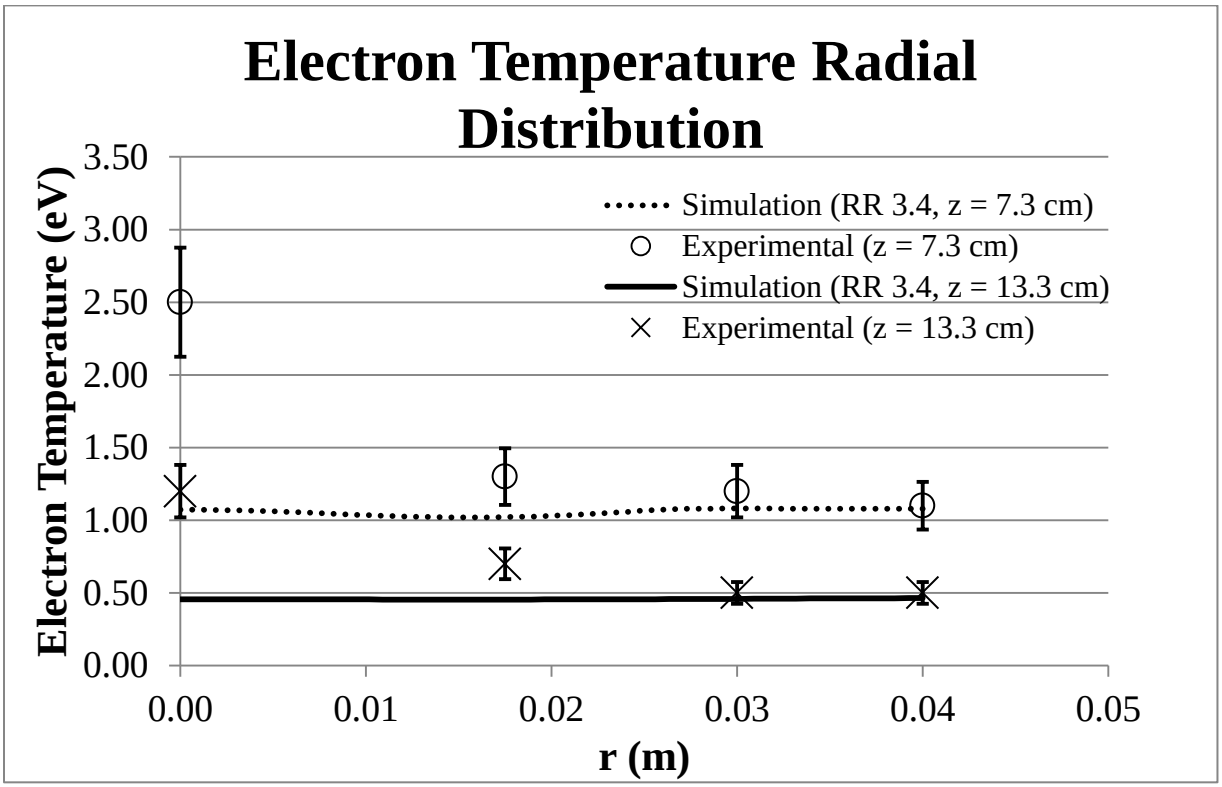


Figure 5.14: Radial variation of electron temperature for simulation (RR = 3.4) and experimental (±15%) values.

Figure 5.15 shows the electron temperature throughout the region of the model. Closer to the exit plane of the thruster, the temperature behavior resembled that of the experimental measurements, with a high temperature at the centerline that dropped in the radial direction. It was thought that the thermal conductivity model might have caused the temperature to normalize further downstream into temperatures lower than experimentally measured. Therefore, getting the correct thermal conductivity setup is one avenue of future work for this model.

Additionally, Figure 5.16 below shows the electron temperature for the radius ratio of 5 case. The electron temperature for the larger radius ratio was higher than the electron temperature for the smaller radius ratio.

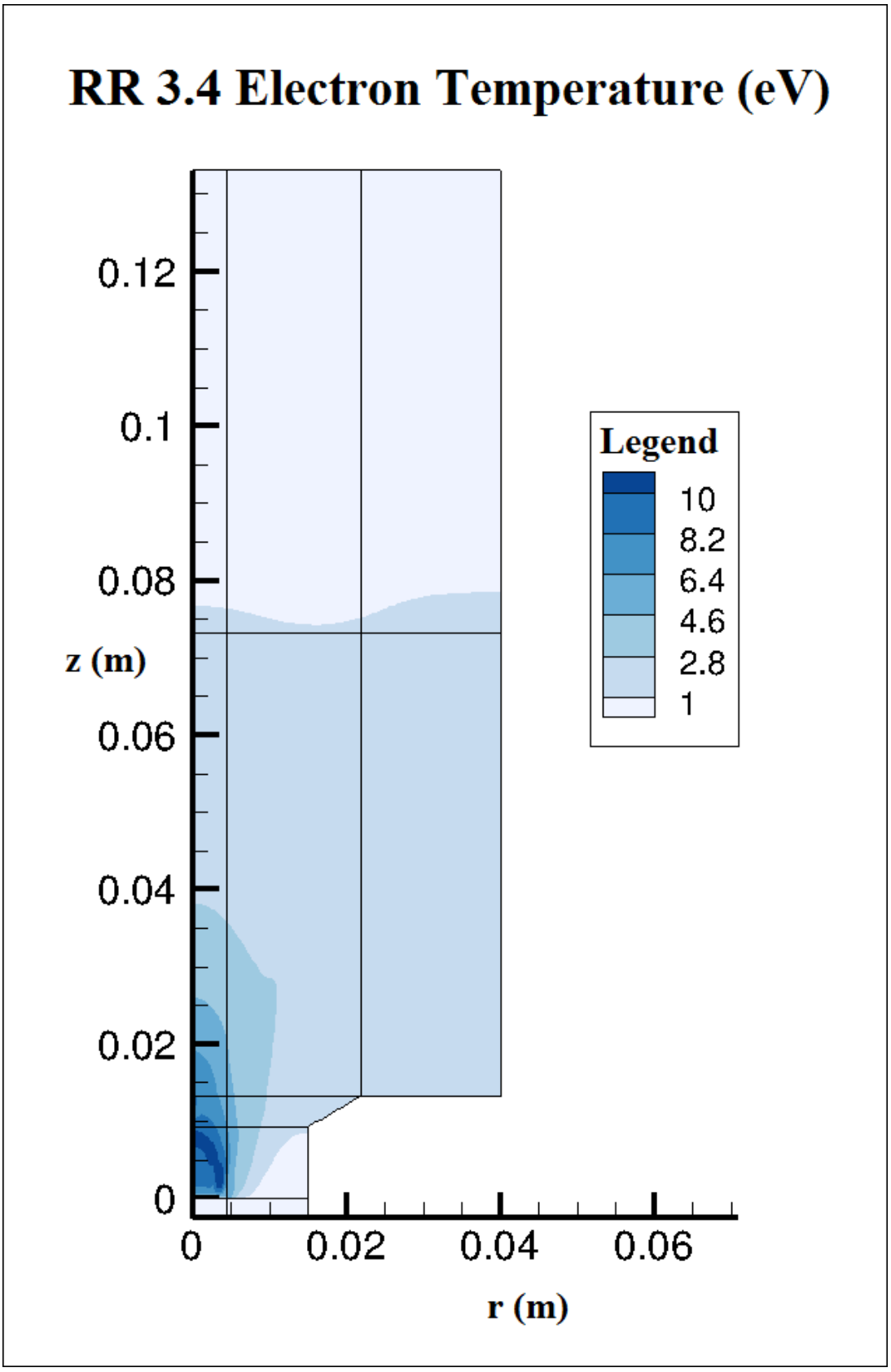


Figure 5.15: Electron temperature contour plot for radius ratio of 3.4.

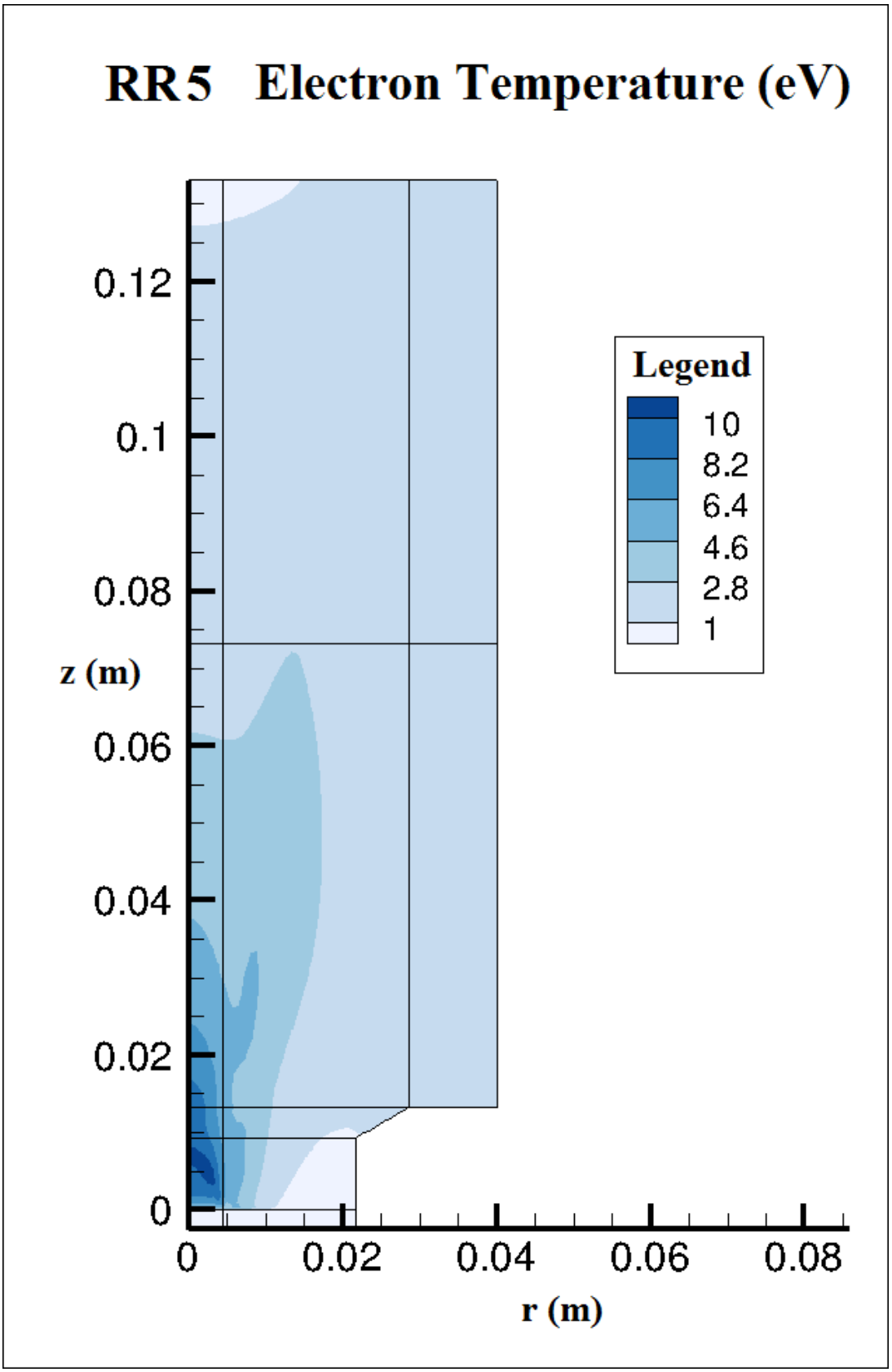


Figure 5.16: Electron temperature contour plot for radius ratio of 5.

Finally, Figure 5.17 is an expanded plot of Figure 5.13 and shows the axial variation of electron and ion temperature for both radius ratios from z = 0 to z = 3.5 cm. Near the cathode, it was seen that the electron and ion temperatures were invariant with the radius ratio, with the electron temperature greater than the ion temperature. Travelling further axially, however, showed the electron and ion temperatures equaling each other for each radius ratio, meaning that the plasma was in equilibrium, with the radius ratio of 5 values higher than the radius ratio of 3.4 values.

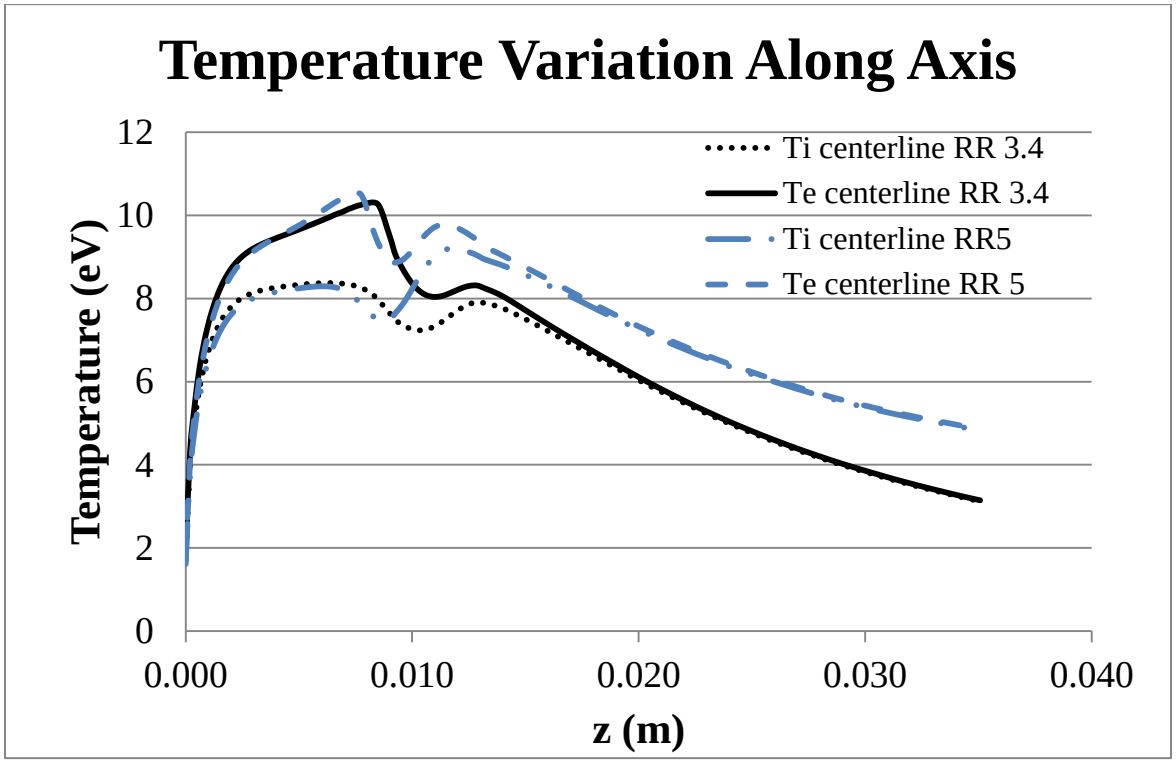


Figure 5.17: Electron and ion temperature variation along axis for both radius ratios. (Expanded plot of Figure 5.13.)

## 5.7 Electrical Conductivity

The electrical conductivity is used in MACH2 in calculating the electric field through Ohm's Law, and it was examined along the axis for both radius ratios, as shown below in Figure 5.18. Corresponding to the electron temperature results, the radius ratio of 5 case had higher

conductivity values than that of the radius ratio of 3.4 case. Peak values along the axis were approximately equal, with the smaller radius ratio having a peak conductivity of 54,700 S/m at z = 8 mm (corresponding to $T_e$ = 10.3 eV), and the larger radius ratio having a peak conductivity of 56,100 S/m at z = 7 mm (corresponding to $T_e$ = 10.5 eV). While a full set of experimental data did not exist for comparison, in the prior experimental study, a conductivity of 7,932 S/m was calculated at z = 3.3 cm. This assumed a Z = 3 plasma and an electron temperature of ~4 eV. While these MACH2 simulations used Z = 2, a similar electron temperature was found, and the conductivity was observed to be 11,900 S/m at this location.

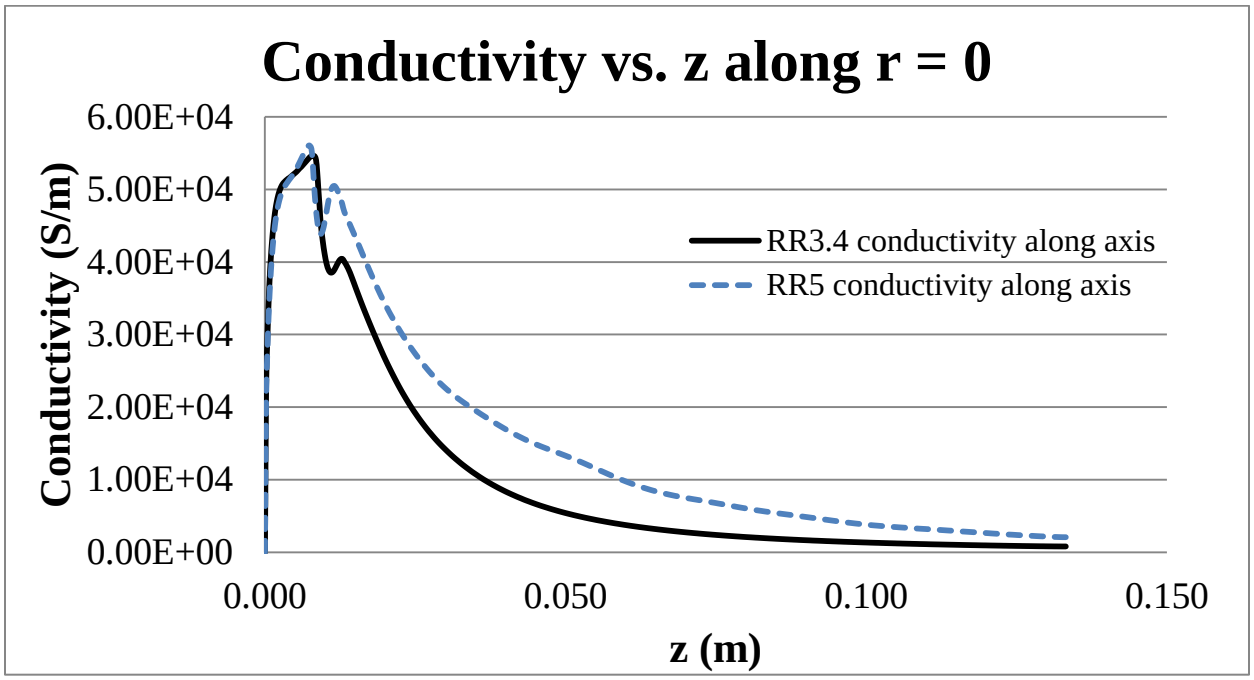

Figure 5.18: Electrical conductivity variation along axis for both radius ratios.

Axial current density was also plotted along the axis for both radius ratios and is shown below in Figure 5.19. The axial current density was shown to be higher for the larger radius ratio than the smaller radius ratio. This might have been due to the current density "flaring out" for the smaller radius ratio as the flow progressed downstream. Overall, it should also be noted that the

electrical conductivity and current density values were in agreement with the aforementioned electric field results.

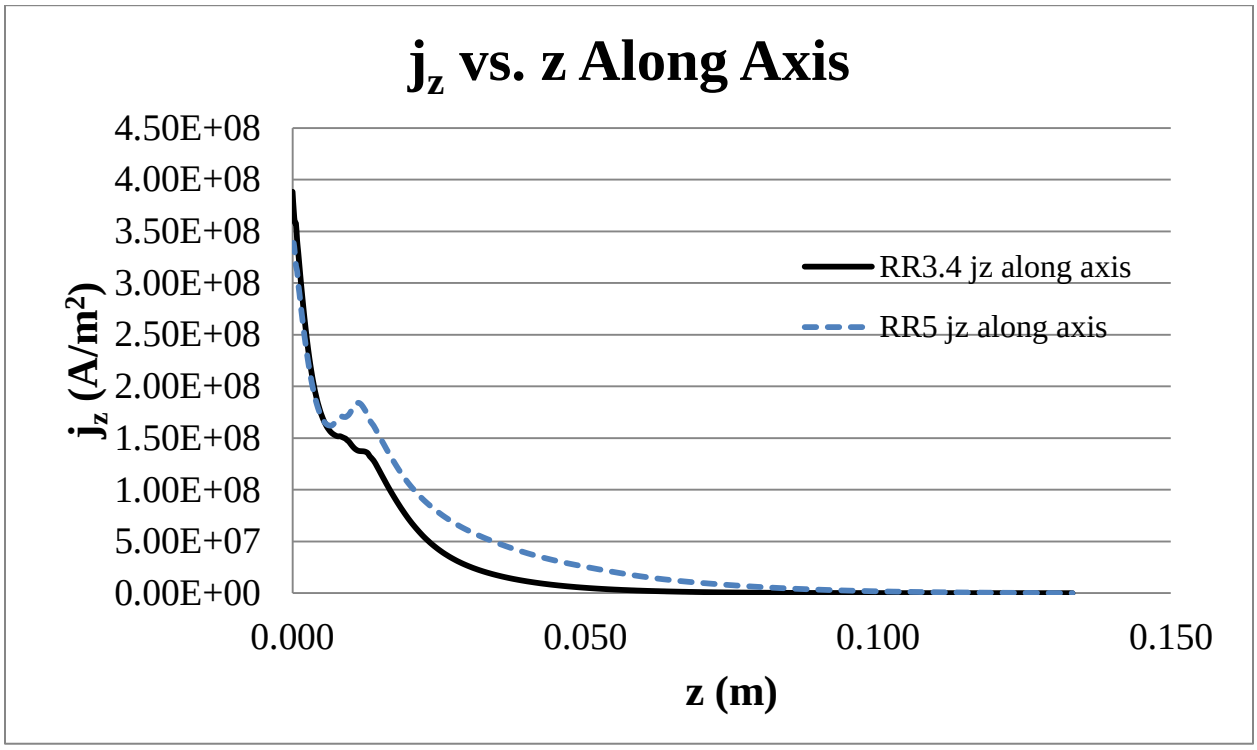


Figure 5.19: Axial current density variation along axis for both radius ratios.

Conductivity data was plotted on a contour plot for both radius ratios and are shown below in Figures 5.20 and 5.21. For the smaller radius ratio, the conductivity was shown to be high near the thruster exit, and it sharply decreased at approximately z = 6 cm. For the larger radius ratio, the conductivity was shown to be higher overall throughout the region.

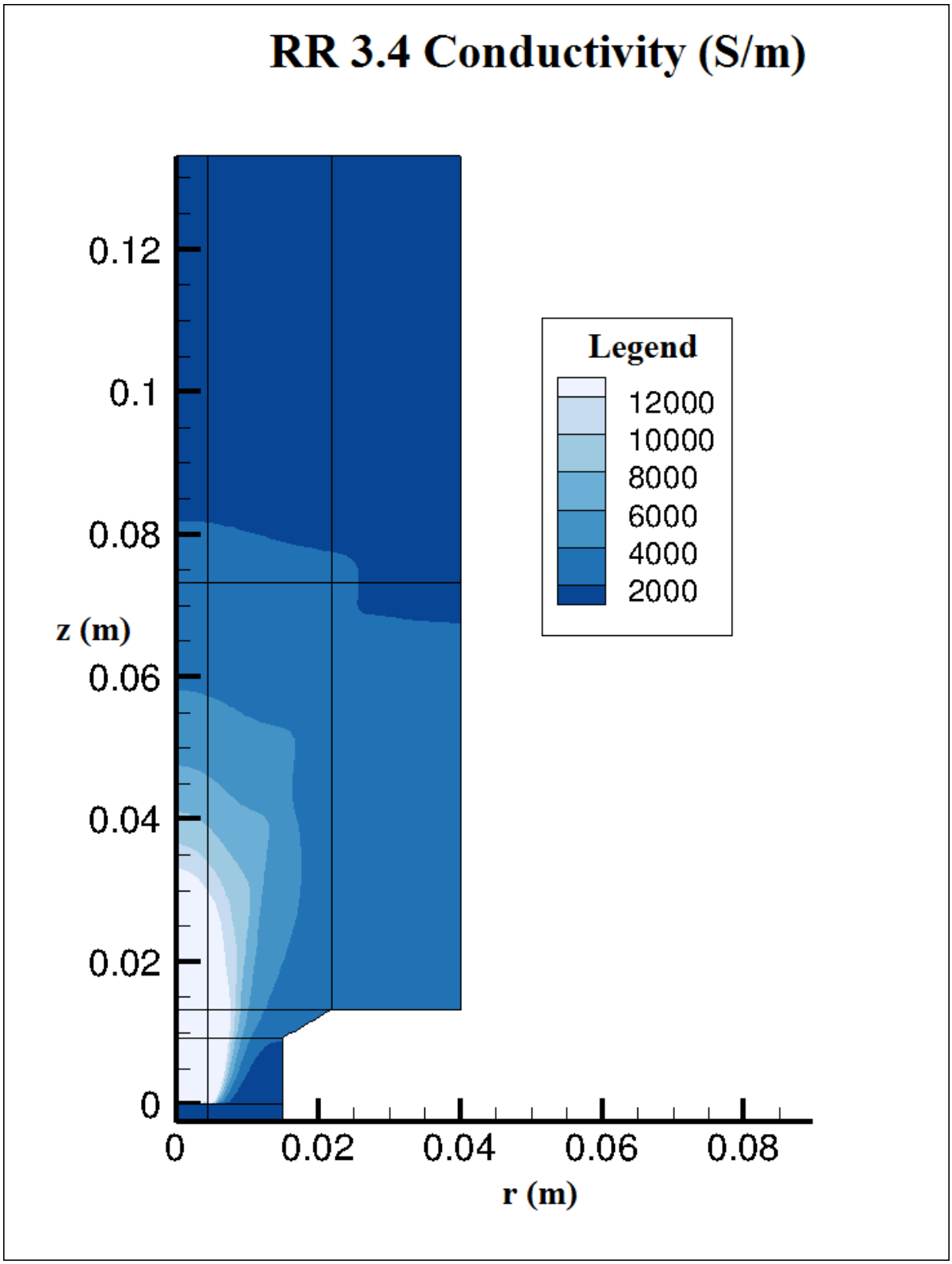


Figure 5.20: Conductivity contour plot for radius ratio of 3.4.

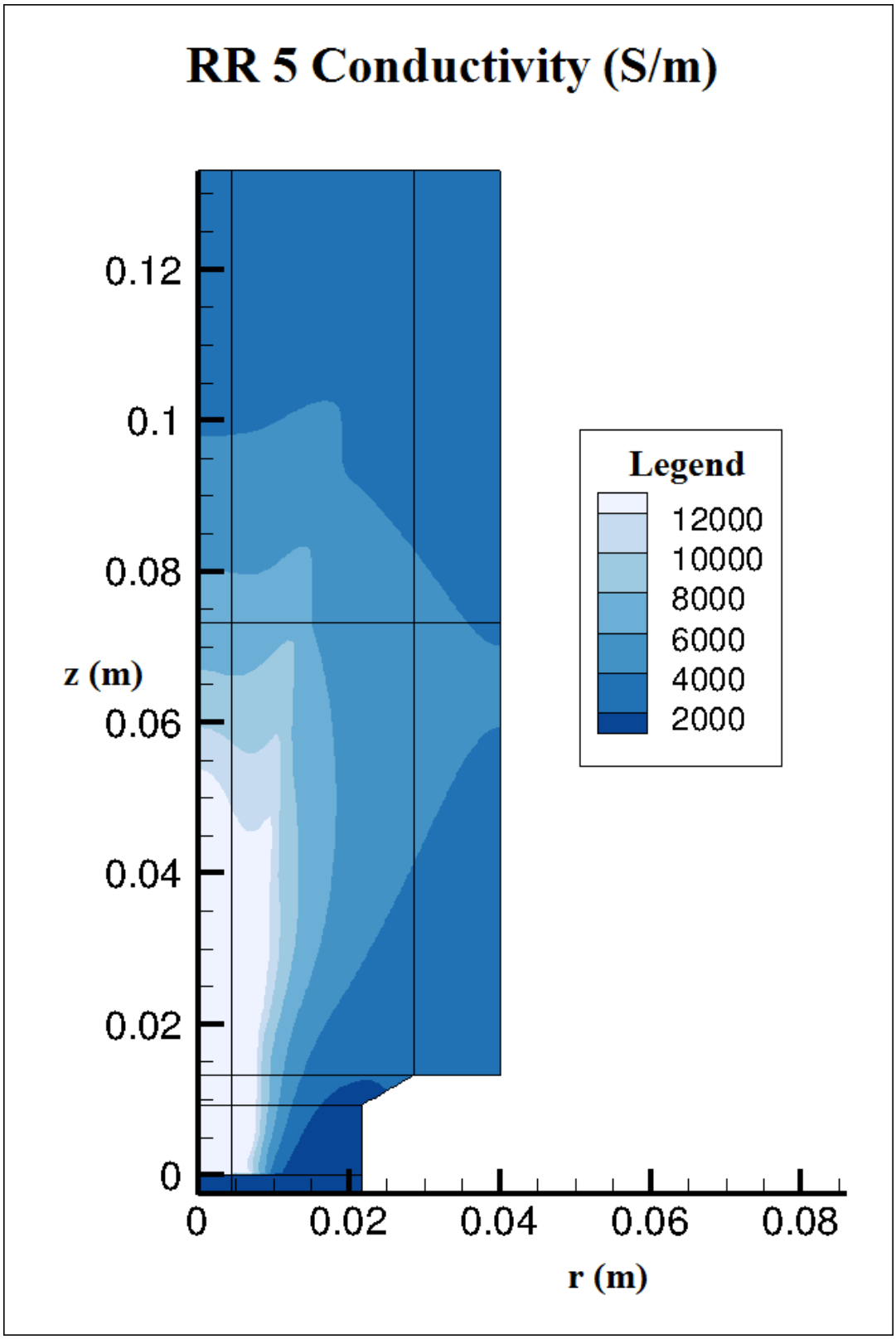


Figure 5.21: Conductivity contour plot for radius ratio of 5.

## 5.8 Velocity Results

Figures 5.22 and 5.23 below show the axial velocity as a function of axial and radial directions, respectively. The axial measurements were taken at r = 0 along the z axis from the face of the cathode to 12 cm from the exit plane of the thruster (z = 13.3 cm). The simulated axial velocities reached an approximate steady value of 17 km/s, with values falling within the experimental error of the crossed probe data. It should be noted that crossed probe experimental data showed a velocity of approximately 22 km/s at z = 19.3 cm (not shown here). While this point on the z axis was not part of the simulation, it can be inferred from the simulation's steady value that the simulation would undershoot this velocity value, though it would likely fall in the ±50% error bar. Thus while the simulation data did not show a significant increase downstream, it still fell within experimental error. In contrast, the simulation's radial distribution did not match experimental values. This was due to computational difficulties in simulating very low density regions.

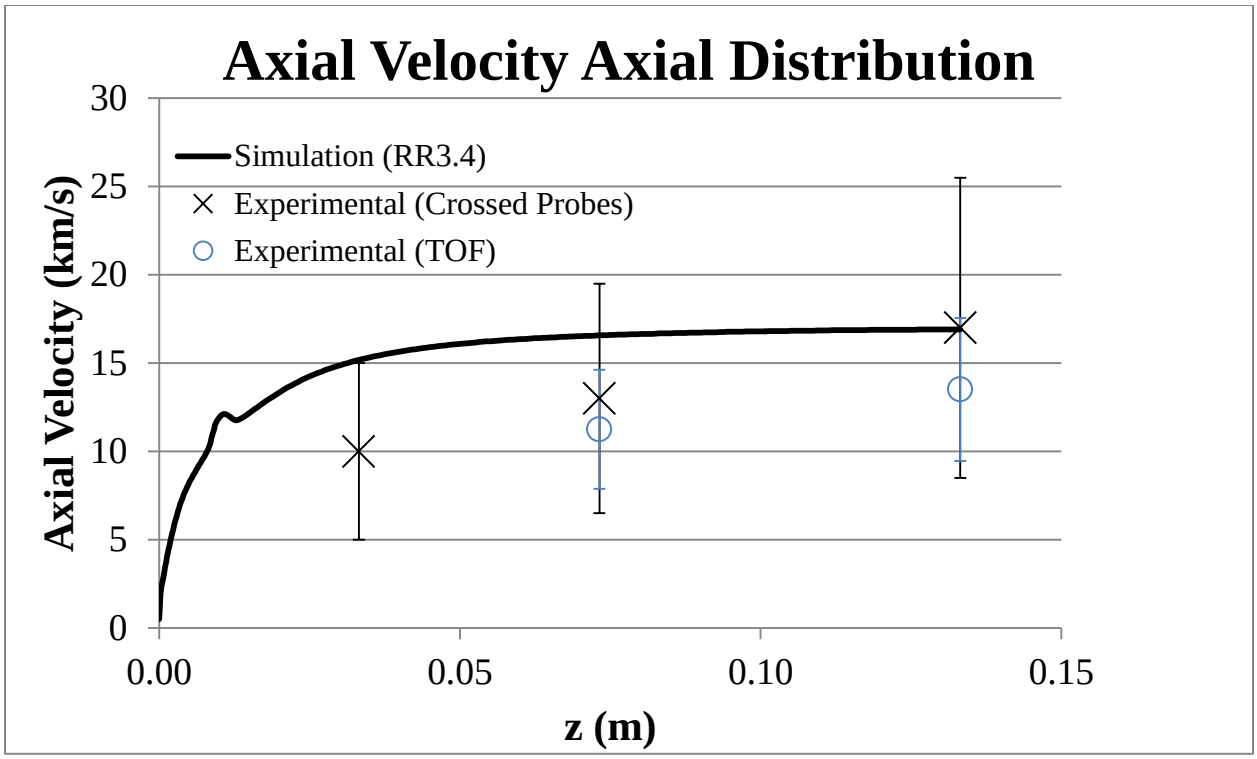


Figure 5.22: Axial variation of axial velocity for simulation and experimental (cross probes: ±50%, TOF: ±30%) values.

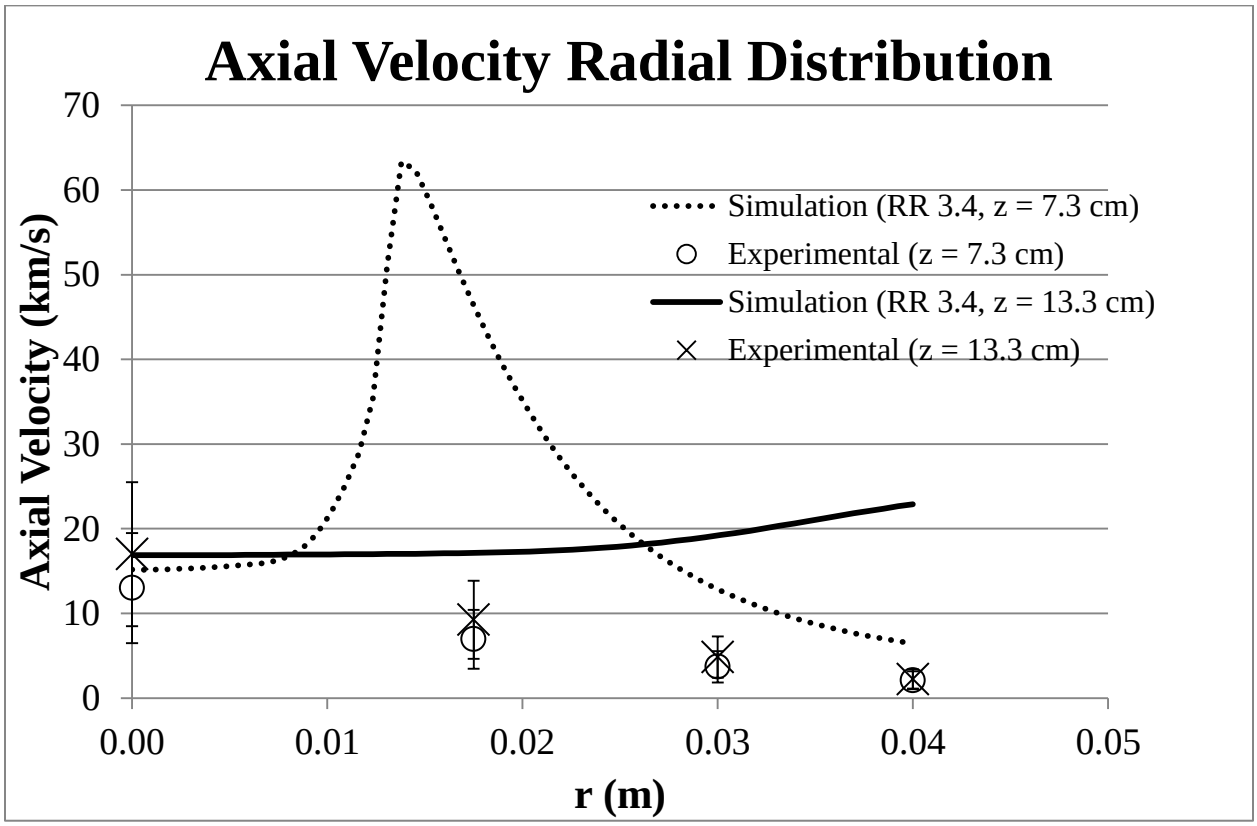


Figure 5.23: Radial variation of axial velocity for simulation and experimental (±50%) values.

Figures 5.24 and 5.25 below show contour plots of the axial and radial velocities (respectively) throughout the model region. Again, the regions of very high velocity corresponded to regions of very low density.

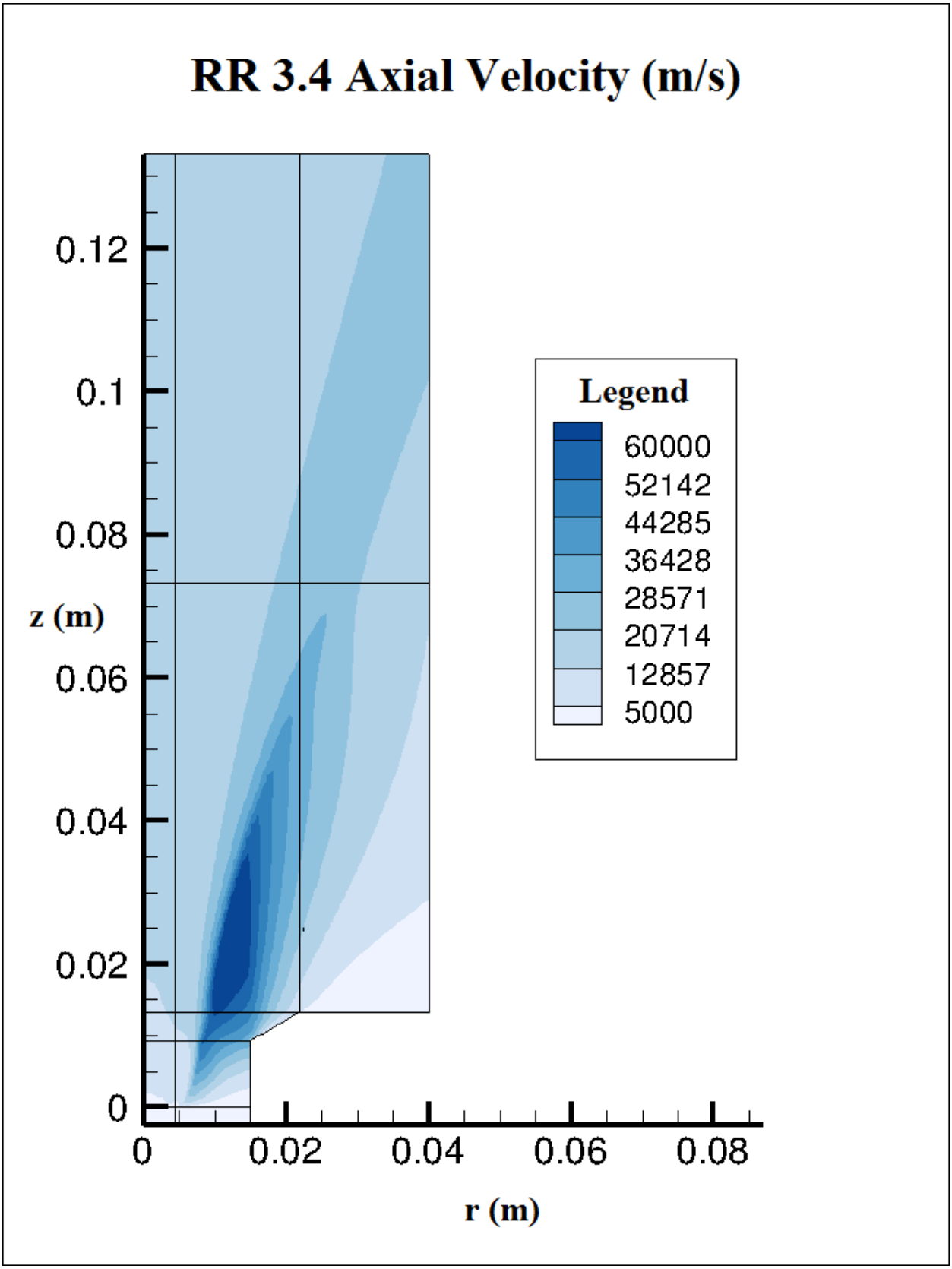


Figure 5.24: Axial velocity contour plot for radius ratio of 3.4.

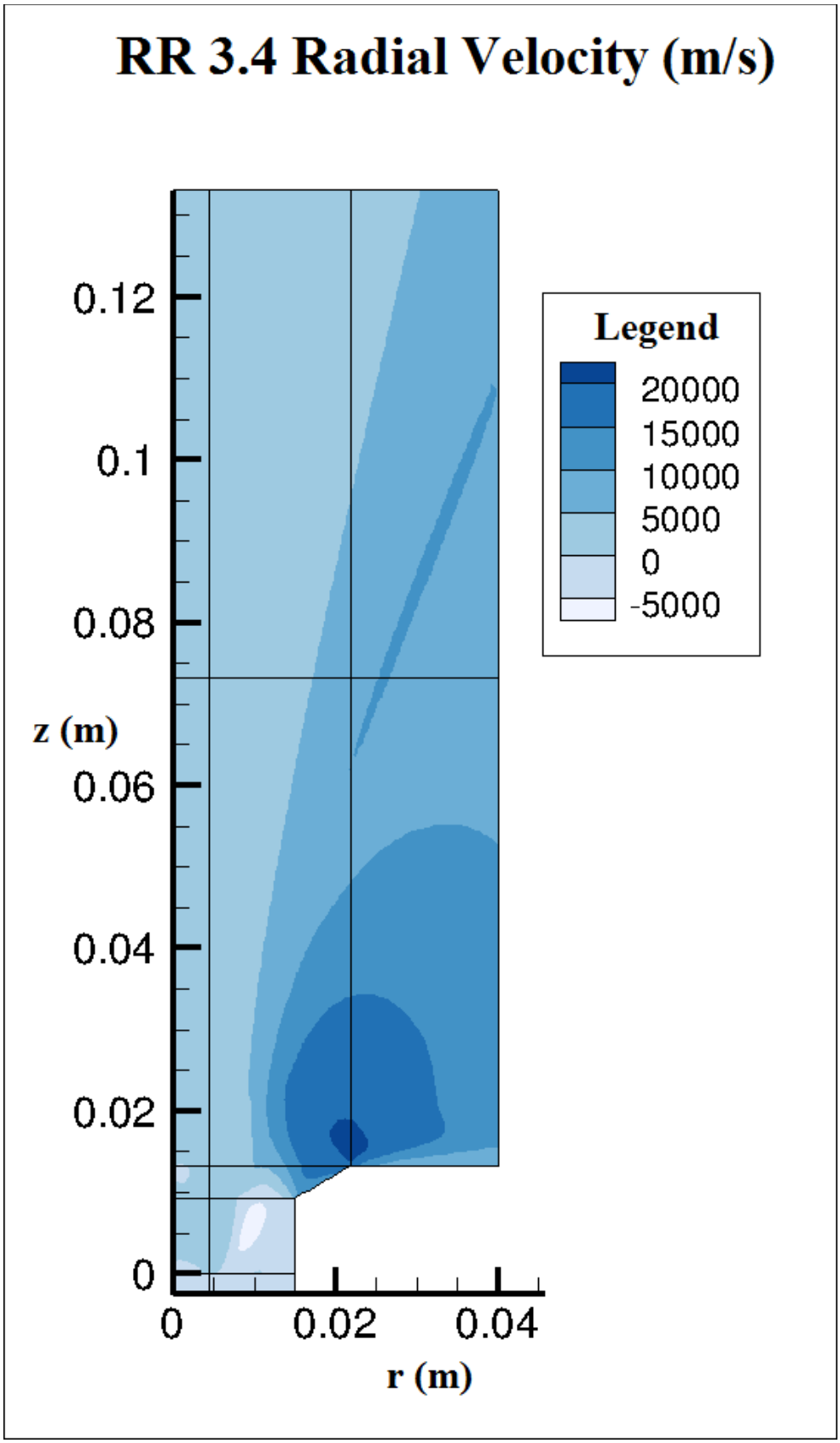


Figure 5.25: Radial velocity contour plot for radius ratio of 3.4.

## 5.9 Mass Flow, Momentum, and Analyses for Varying Radius Ratios

### 5.9.1 Mass Flow and Momentum Flow Rate Calculations

The mass flow rate was measured so as to ensure that the conservation of mass held throughout the thruster and that a mass flow rate of 6 g/s was maintained. Additionally, a momentum flow rate parameter (units of force) was defined as the mass flow across a boundary multiplied by the axial (z direction) velocity at that boundary, and it was derived for comparison with the theoretical MPD thrust values. The mass flow and momentum flow rate were measured at several locations. First, values were obtained across the exit face of the thruster (z = 1.3 cm). Then, sets of values were obtained in axial intervals of 2 cm from this boundary. In addition, these values were also measured along the corresponding radial boundary along blocks 6 and 11.

To calculate the total mass flow rate and momentum flow rate, the mass flow rate and momentum flow rate from each cell along the specified boundary were computed and summed. Specifically, for a cell on a given boundary (i.e., along z = 3.3 cm or r = 2.2 cm), the density and velocity values (axial or radial component, depending on the normal of the cell boundary) were taken from each corner touching the boundary. These values were then averaged to interpolate a value for the middle of the cell. Using these values, the cell's mass flow rate and momentum flow rate were computed as follows:

Mass flow rate:

$$\dot{m}_{axial} = \rho * V_{axial} * \pi * (R^2 - r^2) \quad \text{Axial mass flow rate} \qquad (5.4)$$

$$\dot{m}_{radial} = \rho * V_{radial} * 2\pi * R * h \quad \text{Radial mass flow rate} \qquad (5.5)$$

Momentum flow rate:

$$F_{z,axial} = \dot{m}_{axial} * V_{axial} \quad \text{Axial momentum flow rate} \quad (5.6)$$

$$F_{z,radial} = \dot{m}_{radial} * V_{axial} \quad \text{Radial momentum flow rate} \quad (5.7)$$

where ρ is the density at the midpoint of the corners along the specified boundary, $V_{axial}$ is the midpoint axial velocity, $V_{radial}$ is the midpoint radial velocity, R is the cell's rightmost radius value, r is the cell's leftmost radius value, and h is the height of the cell. The following two equations were then defined:

$$F_{z,total} = F_{z,axial} + F_{z,radial} \quad (5.8)$$

$$\dot{m}_{total} = \dot{m}_{axial} + \dot{m}_{radial} \quad (5.9)$$

Additionally, the exhaust velocity ($U_e$) and specific impulse ($I_{sp}$) were compared at these boundaries. These were calculated as follows:

$$U_e = \frac{F_{z,total}}{\dot{m}_{total}} \quad (5.10)$$

$$I_{sp} = \frac{U_e}{g} \quad (5.11)$$

where g is the gravitational constant 9.81 $m/s^2$.

### 5.9.2 Mass Flow Rate Results

Tables 5.2 and 5.3 below show the mass flow rate for RR 3.4 and RR 5 as a function of z. In these cases, the axial mass flow rate decreased as z increased, and the radial mass flow rate

increased, keeping the total mass flow rate approximately constant. The boundaries at z = 7.3 cm marked where the flow became approximately constant in space as it moved downstream. Between the two radius ratios, the RR 3.4 case had more radially outward mass flow downstream compared to the RR 5 case. This might have been due to the larger total axial Lorentz force for the RR 5 case. In summary, both cases had nominal total mass flow rates of 6 g/s.

Table 5.2: Mass flow rate for RR 3.4 (25 μs).

| z (m) | Axial mass flow rate (g/s) | Radial mass flow rate (g/s) | Total mass flow rate (g/s) |
|---|---|---|---|
| 0.013 | 5.95 | N/A | 5.92 |
| 0.033 | 5.81 | 0.25 | 6.06 |
| 0.053 | 5.67 | 0.42 | 6.09 |
| 0.073 | 4.69 | 1.39 | 6.08 |
| 0.093 | 3.03 | 3.04 | 6.07 |
| 0.113 | 2.06 | 4.01 | 6.08 |
| 0.133 | 1.48 | 4.60 | 6.08 |

Table 5.3: Mass flow rate for RR 5 (25 μs).

| z (m) | Axial mass flow rate (g/s) | Radial mass flow rate (g/s) | Total mass flow rate (g/s) |
|---|---|---|---|
| 0.013 | 5.41 | N/A | 5.41 |
| 0.033 | 5.42 | 0.30 | 5.72 |
| 0.053 | 5.29 | 0.57 | 5.86 |
| 0.073 | 5.24 | 0.78 | 6.02 |
| 0.093 | 5.12 | 0.92 | 6.05 |
| 0.113 | 5.09 | 1.01 | 6.09 |
| 0.133 | 4.94 | 1.15 | 6.08 |

### 5.9.3 Theoretical MPD Thrust Values

The axial force due to the **j** x **B** force for a gas-fed MPD thruster is given by Jahn [2]:

$$F_z = \frac{\mu_0 I^2}{4\pi}\left(\ln\frac{r_a}{r_c} + C\right) \quad (5.12)$$

where $\mu_0$ is the vacuum permeability [$4*\pi*10^{-7}$ (V-s)/(A-m)], I is the current, $r_a$ is the anode radius, $r_c$ is the cathode radius, and C is a constant relating to the geometry of the cathode (for this study C = 0.5, which corresponds to a flat cathode surface). The predicted thrust values are shown below in Table 5.4. Note that in addition, an electrothermal component of thrust not accounted for in the above equation has been demonstrated to exist [1].

Table 5.4: Predicted Jahn thrust values for varying radius ratio, with current = 22.6 kA.

| Radius Ratio | $F_z$ (N) |
|---|---|
| 3.4 | 89 |
| 5 | 108 |

### 5.9.4 Momentum Flow Rate Results

Tables 5.5 and 5.6 below show the momentum flow rate, $U_e$, and $I_{sp}$ data for RR 3.4 and RR 5 as functions of z. At z = 7.3 cm, the total momentum flow rate for the RR 3.4 case was 124 N, in comparison to that of the RR 5 case, which was 131 N. Compared with theoretical values, the simulated thrust values were higher. This indicated the existence of an electrothermal thrust component not accounted for in the theoretical prediction. The results also indicated that though the increased radius ratio resulted in a higher thrust, the difference was not as high as predicted (7 N vs. 19 N).

Table 5.5: Momentum flow rate, $U_e$, and $I_{sp}$ data for RR 3.4 (25 μs).

| z (m) | Total momentum flow rate (N) | $U_e$ (km/s) | $I_{sp}$ (s) |
|---|---|---|---|
| 0.013 | 106 | 17.9 | 1825 |
| 0.033 | 121 | 19.9 | 2029 |
| 0.053 | 123 | 20.2 | 2058 |
| 0.073 | 124 | 20.4 | 2084 |
| 0.093 | 125 | 20.6 | 2103 |
| 0.113 | 126 | 20.7 | 2110 |
| 0.133 | 126 | 20.7 | 2111 |

Table 5.6: Momentum flow rate, $U_e$, and $I_{sp}$ data for RR 5 (25 μs).

| z (m) | Total momentum flow rate (N) | $U_e$ (km/s) | $I_{sp}$ (s) |
|---|---|---|---|
| 0.013 | 106 | 19.6 | 1999 |
| 0.033 | 128 | 22.3 | 2274 |
| 0.053 | 130 | 22.1 | 2252 |
| 0.073 | 131 | 21.8 | 2221 |
| 0.093 | 131 | 21.6 | 2206 |
| 0.113 | 132 | 21.7 | 2207 |
| 0.133 | 132 | 21.7 | 2208 |

Plots were generated showing the axial momentum (density multiplied by axial velocity) for both radius ratios. These plots are shown below in Figures 5.26 and 5.27, and they show what was described above: for the radius ratio of 3.4, the axial momentum decreased more quickly downstream than that of the radius ratio 5. Additionally, as stated before, velocity values for regions of low density were extremely high, however because of the low density, the overall effect on the momentum was negligible.

Plots were also generated showing the axial momentum across the z = 7.3 cm and z = 13.3 cm boundaries for both radius ratios. These plots are shown below in Figures 5.28 and 5.29. The larger radius ratio had higher values of axial momentum compared to the smaller radius ratio. Additionally, overall, the axial momentum of the larger radius ratio was more tightly held to the axis than that of the smaller radius ratio, as the smaller radius ratio showed a greater radial expansion.

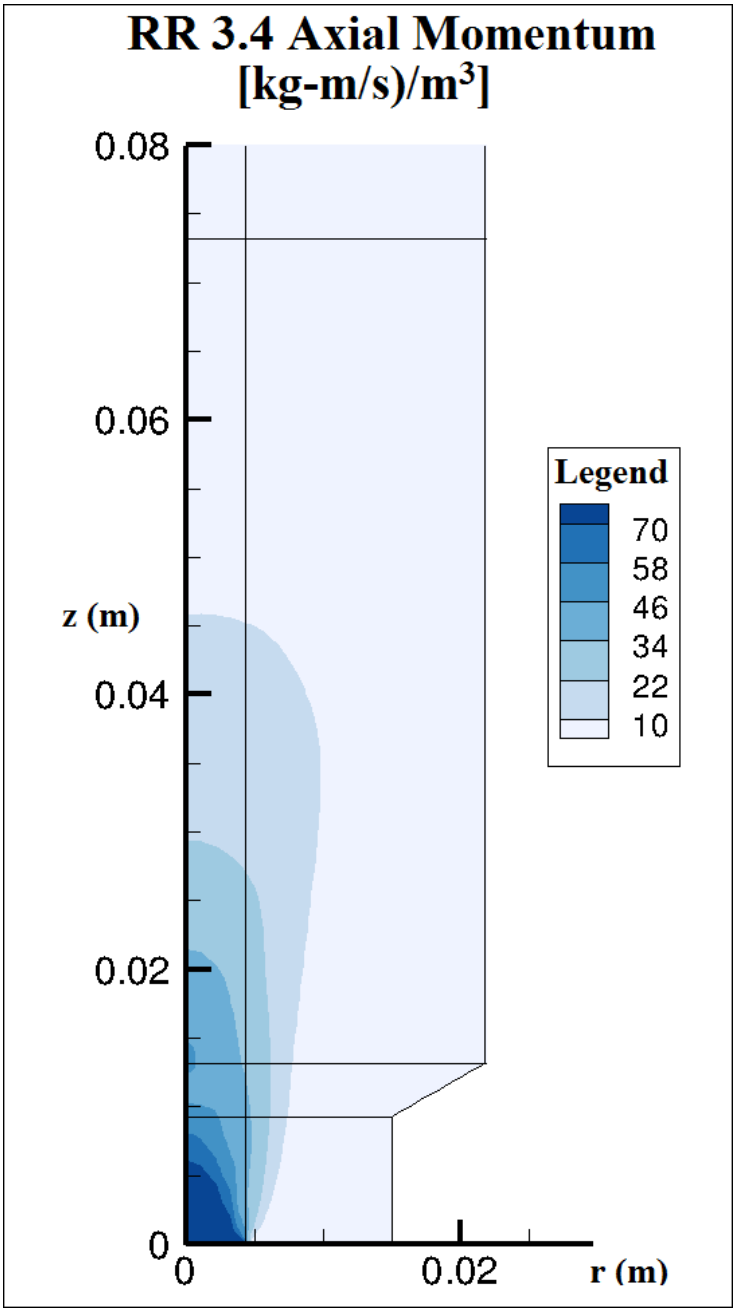

Figure 5.26: Axial momentum contour plot for radius ratio of 3.4.

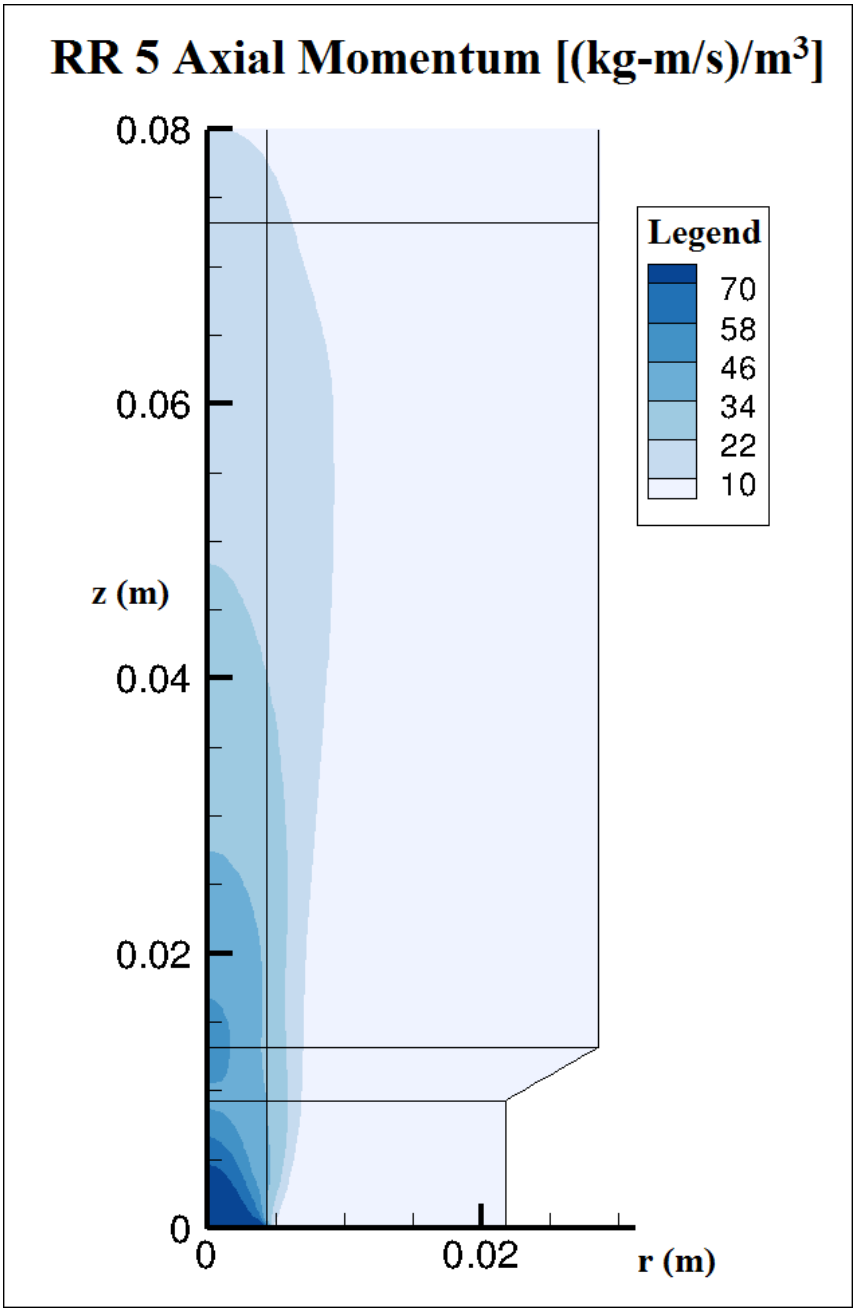

Figure 5.27: Axial momentum contour plot for radius ratio of 5.

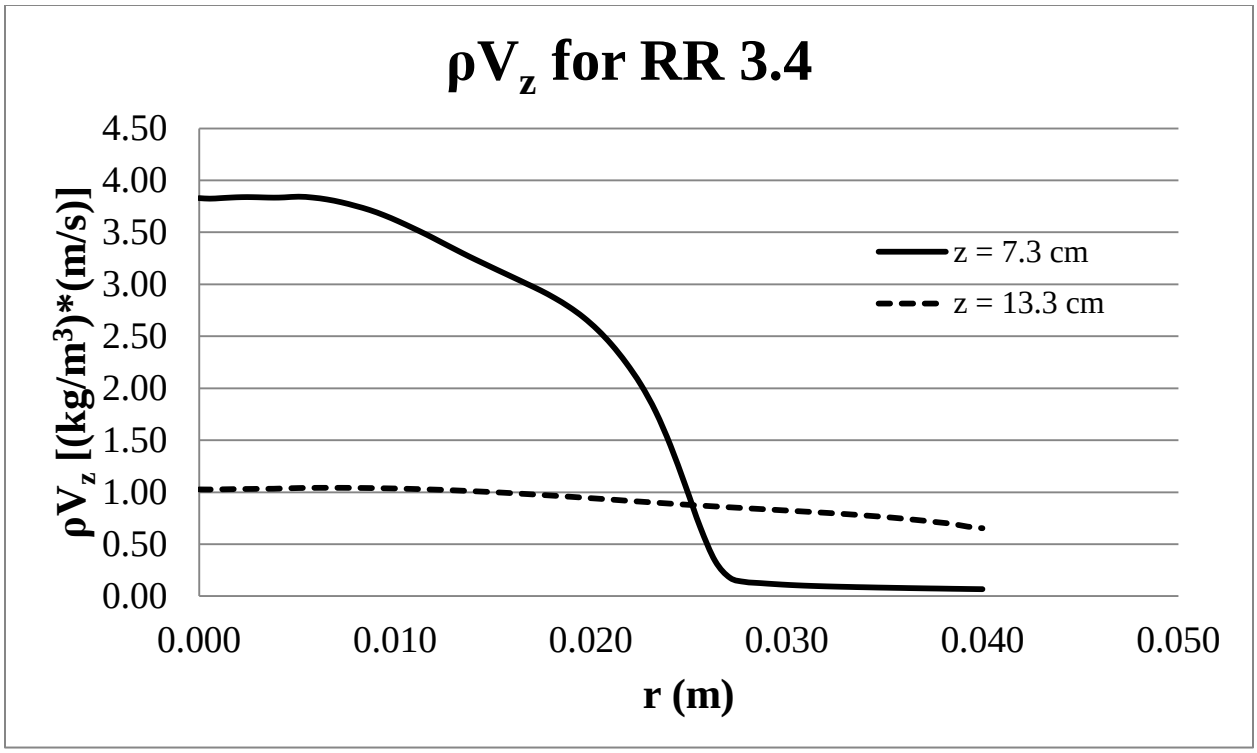


Figure 5.28: Axial momentum across z = 7.3 cm and z = 13.3 cm boundaries for radius ratio of 3.4.

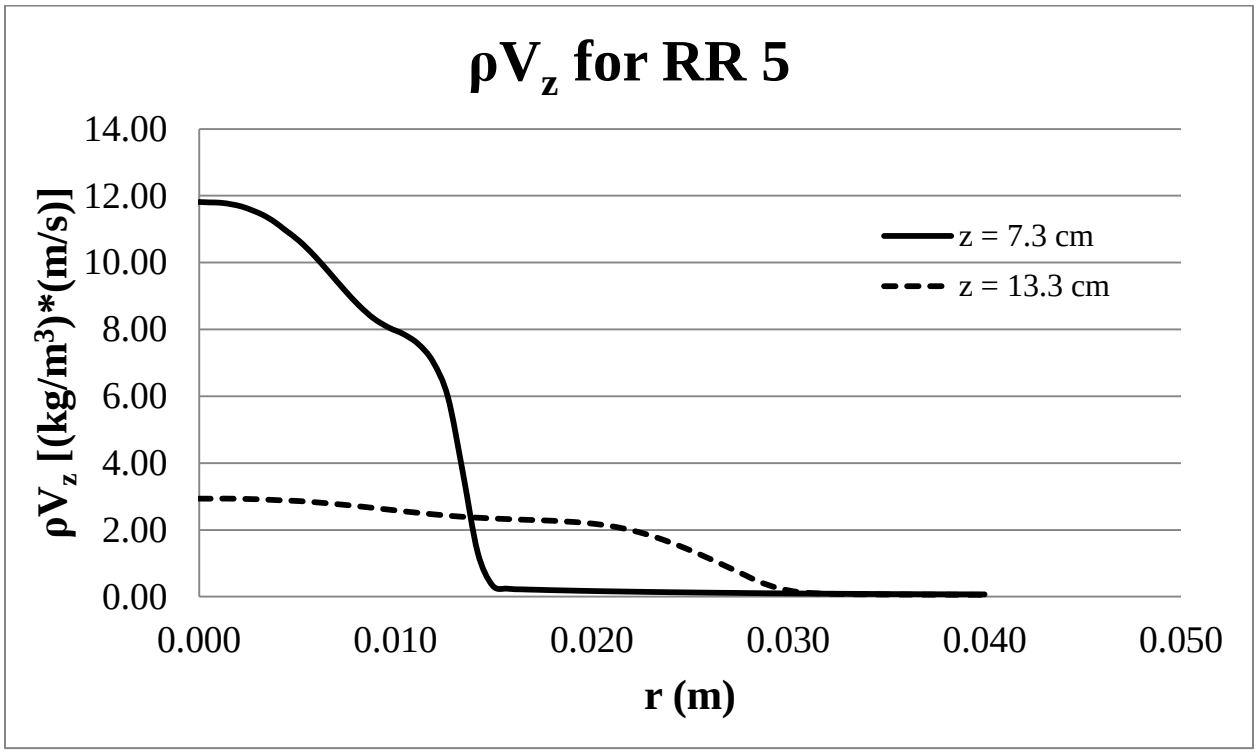


Figure 5.29: Axial momentum across z = 7.3 cm and z = 13.3 cm boundaries for radius ratio of 5.

Plots were also generated of the axial momentum multiplied by the axial velocity, and they are shown below in Figures 5.30 and 5.31. These were generated across the z = 7.3 cm and z = 13.3 cm boundaries for both radius ratios, and these plots indicated the amount of energy being transferred across the boundaries. Similar to the axial momentum plots across these boundaries, the larger radius ratio had higher values compared to the smaller radius ratio, and the smaller radius ratio showed more radial expansion.

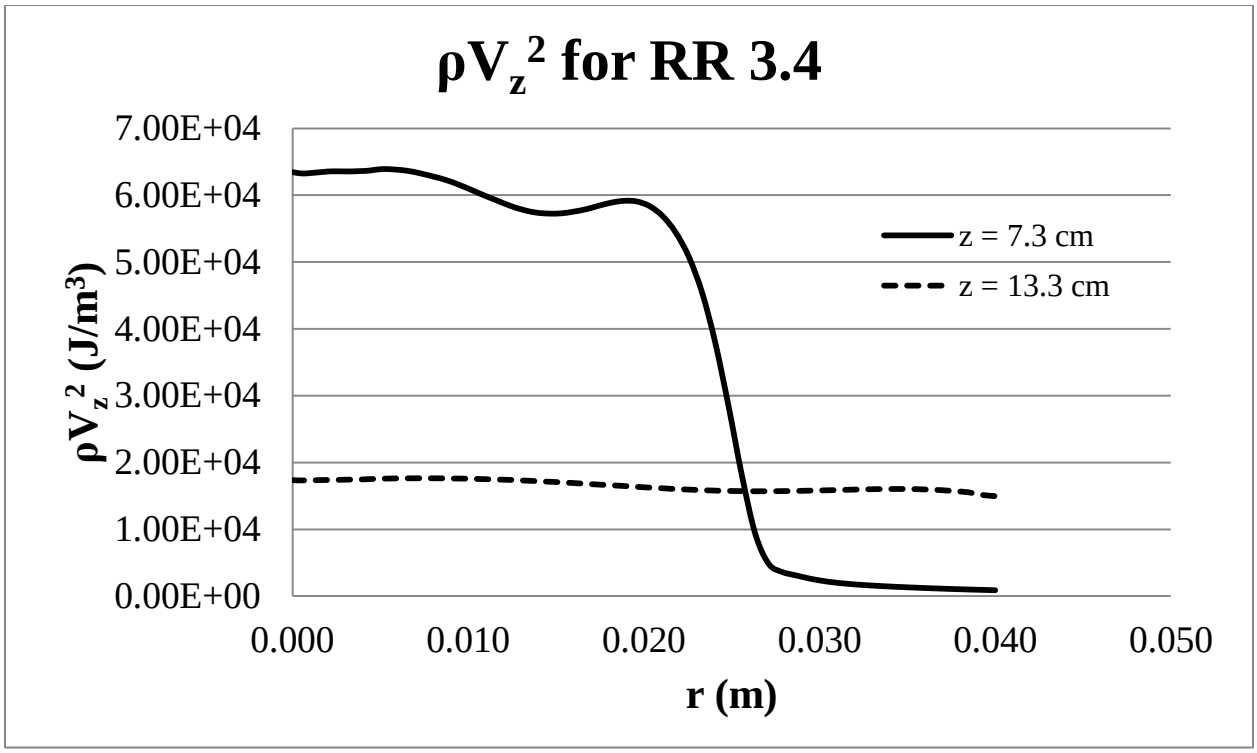


Figure 5.30: Axial momentum multiplied by axial velocity across z = 7.3 cm and z = 13.3 cm boundaries for radius ratio of 3.4.

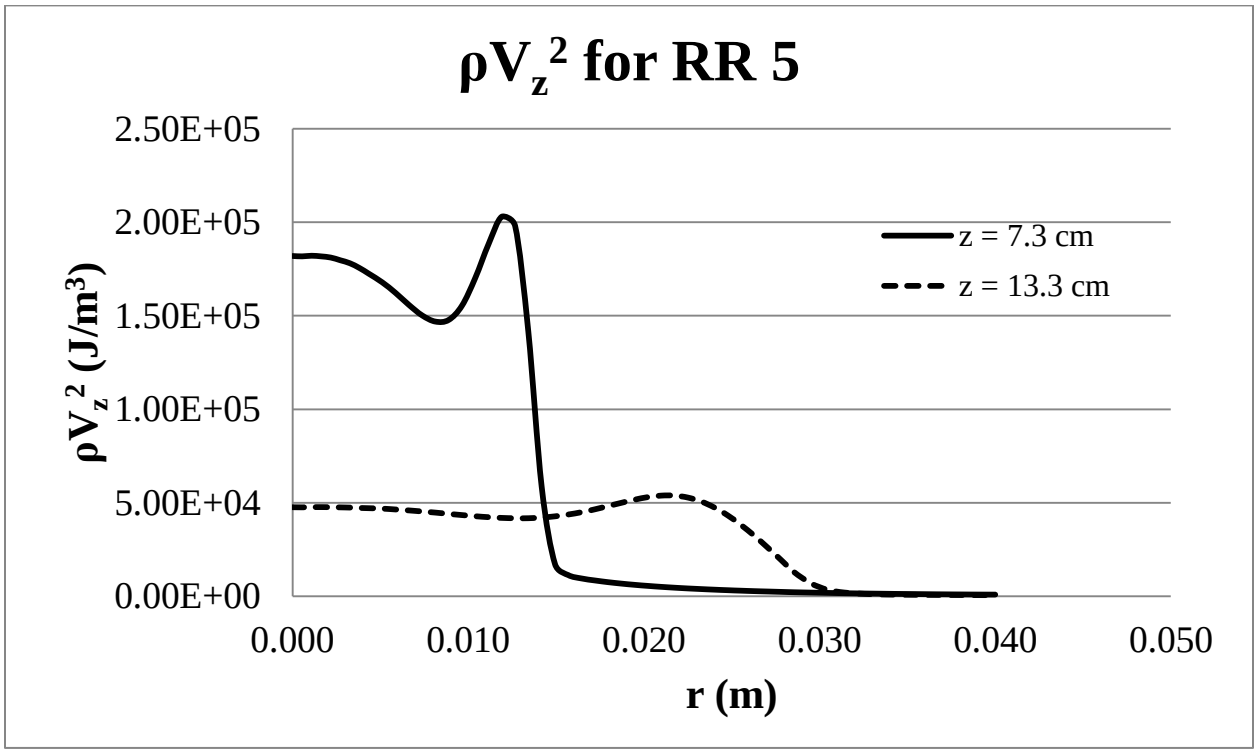


Figure 5.31: Axial momentum multiplied by axial velocity across z = 7.3 cm and z = 13.3 cm boundaries for radius ratio of 5.

### 5.9.5 Explanation of Potential Issues Regarding Mass Flow Boundary Conditions

To summarize the final result, the simulations produced a mass flow rate of 6 g/s (matching the experimental mass flow rate) for both the RR 3.4 and RR 5 cases, and the momentum flow rate for the RR 5 case was slightly higher than the RR 3.4 case, matching general theoretical predictions for an MPD thruster. However, an explanation of potential issues involved with the mass flow rate and momentum flow rate calculations is warranted, as it was unknown if the radius ratio increase was the sole reason for this momentum flow rate increase, or if slight differences in the mass flow rates might have been the cause.

As mentioned earlier, there was difficulty in setting the mass flow rate boundary conditions – the density and velocity boundary conditions at the cathode face did not match the input conditions. Additionally, having mass flow boundary conditions on the cathode resulted in flow that did not expand out to the anode radius: the flow did not interact with the magnetic field closer to the anode, and thus changing the radius ratio resulted in the same thrust for different radius ratios. It should be noted that this lack of expansion might have been accurate, since experimental results showed that spoking (visible chaotic current arcing) occurred at a radius ratio of 5 [6]. This might indicate that the mass flow was not supposed to reach the anode for a radius ratio of 5. However, while this physical reason might hold some merit, it is also very likely that there was a computational reason (i.e., a boundary condition) inhibiting this flow out to the anode. Thus, as described above, an insulator mass flow boundary condition was devised.

In adding this insulator mass flow, it was necessary to make sure the insulator mass flow rate was the same for each radius ratio so as to ensure any differences in flow behavior could only be attributed to the changed radius ratio. Thus cases were run for both without the insulator mass

flow and with the insulator mass flow, and the insulator contribution was then be measured by subtraction. At 10 μs for the RR 3.4 case with no insulator mass flow, the simulation appeared steady, and mass flow and thrust values were taken at z = 7.3 cm (6 cm from the exit plane of the thruster). This location was chosen as a benchmark for which to compare values, as it marked the line at which the flow values became approximately constant moving downstream. For the RR 5 case, values were taken along z = 7.3 at 15 μs, as there was more volume for the fluid to travel. Once these mass flow rate and momentum flow rate values for the different radius ratios were observed to be the same, insulator mass flow boundary conditions were added to the insulator until the total mass flow rate equaled approximately 6 g/s for both radius ratios.

These initial simulations were performed on a smaller model than the final model (the exhaust region did not extend as far downstream). Once these 6 g/s mass flow results were obtained for the smaller models, larger models were implemented, and a run time was set to 50 μs to give sufficient time for the flow to travel downstream. For the RR 3.4 and RR 5 cases with the insulator mass flow boundary conditions, the total mass flow rate was 6 g/s, and values were taken at 25 μs (steady state). However for the RR 3.4 and RR 5 cases with the insulator mass flow *off*, it was observed that steady state was never reached – the axial velocity slowly decreased. This might have been due to the boundary conditions placed on the insulator face. This unsteady behavior was originally not seen in the original simulations since the flow region was smaller and the run time was shorter, making it only appear that steady state had been reached.

It should be emphasized that a steady, total mass flow rate of 6 g/s was achieved for both RR 3.4 and RR 5, using an insulator mass flow. The only potential issue is that there was a degree of

uncertainty associated with how much mass was being injected through the insulator mass flow boundary. This raised the question about whether the momentum flow rate difference between the radius ratios was due to the radius ratio, the insulator mass flow rate, or both.

As stated before, values at z = 7.3 cm were used for comparison purposes, as z = 7.3 cm marked where the flow became approximately constant in space as it moved downstream. Table 5.7 below shows values at z = 7.3 cm for the cases with no insulator mass flow along with the cases with an insulator mass flow. With no insulator mass flow, the total mass flow rates and total momentum flow rates for both radius ratios were approximately equal, as described above. For the RR 3.4 case, at z = 7.3 cm, the overall insulator mass flow contribution was measured to be 0.77 g/s, and for the RR 5 case, at z = 7.3 cm, the overall insulator mass flow contribution was measured to be 0.82 g/s. Thus the insulator mass flow rates were approximately equal, and the two sets of data were comparable.

Table 5.7: Mass flow rate and momentum flow rate data at z = 7.3 cm for all cases.

| Case | Axial mass flow rate (g/s) | Radial mass flow rate (g/s) | Total mass flow rate (g/s) | Total momentum flow rate (N) |
|---|---|---|---|---|
| RR 3.4, no insulator mass flow | 3.73 | 1.58 | 5.31 | 90 |
| RR 5, no insulator mass flow | 4.62 | 0.59 | 5.20 | 92 |
| RR 3.4, with insulator mass flow | 4.69 | 1.39 | 6.08 | 124 |
| RR 5, with insulator mass flow | 5.24 | 0.78 | 6.02 | 131 |

# Chapter 6 Analysis and Conclusions

## 6.1 Efficiency Calculations

The efficiency can be calculated as follows:

$$\eta = \frac{{F_{z,total}}^2}{2\dot{m}_{total} VI} \tag{6.1}$$

where $F_{z,total}$ is the total momentum flow rate, $\dot{m}_{total}$ is the total mass flow rate, V is the voltage, and I is the current. These values are summarized below in Table 6.1.

Table 6.1: Efficiency results.

| | Total mass flow rate (g/s) | Total momentum flow rate (N) | Current (kA) | Voltage (V) | η |
|---|---|---|---|---|---|
| RR 3.4 | 6.08 | 124 | 22.6 | 148 | 38% |
| RR 5 | 6.02 | 131 | 22.6 | 222 | 28% |

For the RR 3.4 case, an efficiency of 38% was higher than the 25% measured. This was largely due to the relatively high momentum flow rate of 124 N. Though the theoretical value of 89 N predicted by Jahn does not include electrothermal effects, the 124 N value was likely too high due to approximations made in the code. For the RR 5 case, an efficiency of 28% matched well with the predicted efficiency of 30% [6], though the predicted efficiency assumed electrical characteristics similar to the experimental RR 3.4 case. This was shown in the simulations not to hold, as the voltage increased for the larger radius ratio. This discrepancy in voltage between the predicted and MACH2 efficiencies was likely offset by the momentum flow rate being 131 N, vs. the 108 N value predicted by Jahn.

## 6.2 Heating Effects

In addition to the analysis of the force acting on the cathode due to the pressure there (see Section 5.5), which indicated the presence of electrothermal effects, an analysis of the enthalpy was performed. Several components of enthalpy were examined and are defined below:

$$h_i = \frac{5}{2} R_{Ga} T_i \qquad \text{Specific enthalpy due to ions} \qquad (6.2)$$

$$h_e = 5 R_{Ga} T_e \qquad \text{Specific enthalpy due to electrons} \qquad (6.3)$$

$$h_{total} = h_i + h_e + \frac{v^2}{2} \qquad \text{Total specific enthalpy} \qquad (6.4)$$

where $R_{Ga}$ is the gallium specific gas constant of 119 J/(kg-K), $T_i$ is the ion temperature, $T_e$ is the electron temperature, and v is the axial velocity. These components were analyzed along the axis, and plots of them are shown below in Figures 6.1 and 6.2. The ion and electron specific enthalpies drop after this region, though the enthalpies for the RR 5 case drop more slowly. The total enthalpies are also approximately constant, with the RR 3.4 case having a slightly higher total enthalpy. These figures show a large amount of heating in the thruster from the region z = 0 to approximately z = 1 cm, indicating a large electrothermal effect.

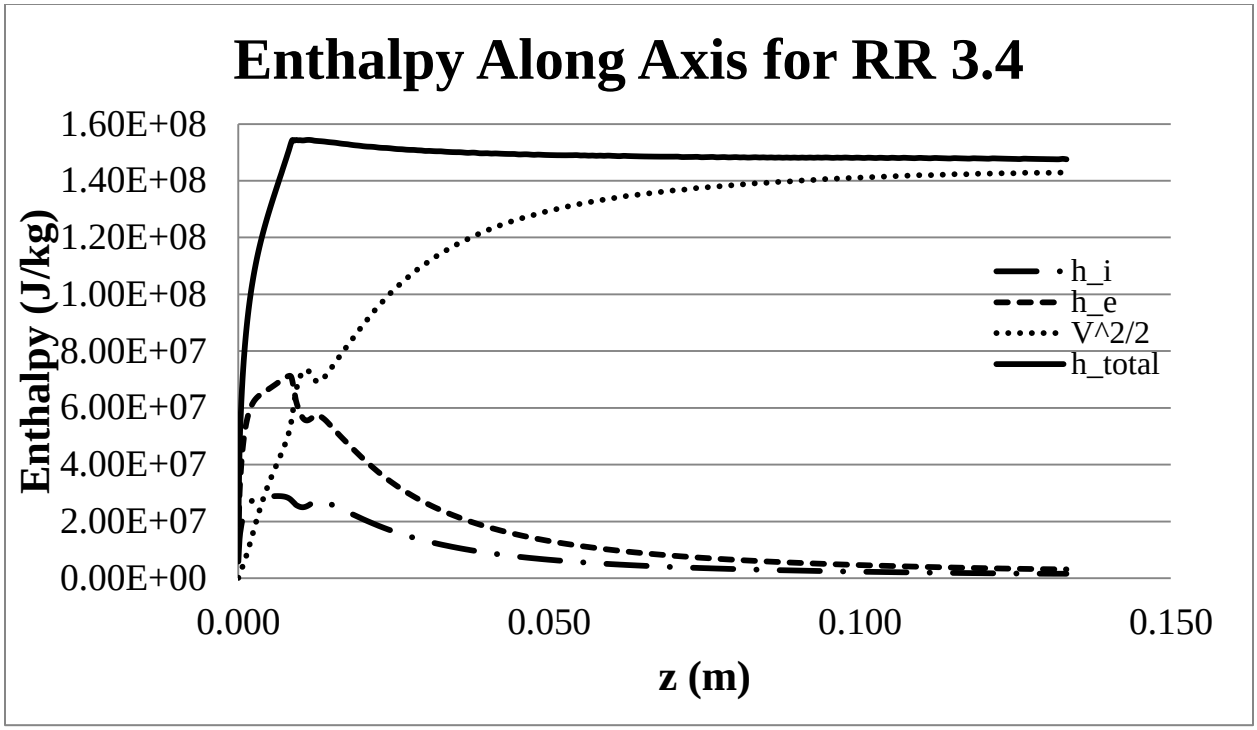


Figure 6.1: Specific enthalpy along axis for RR 3.4.

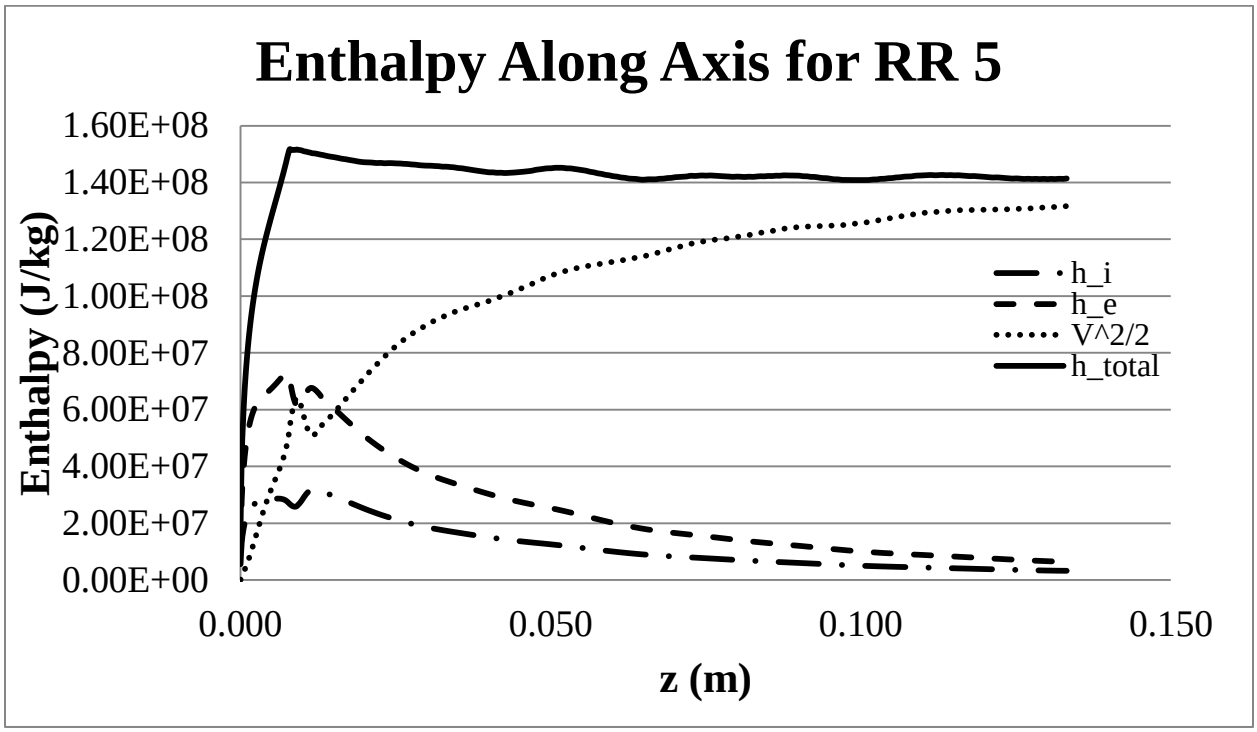


Figure 6.2: Specific enthalpy along axis for RR 5.

The amount of joule heating was also examined along the axis, and a plot of it is shown below in Figure 6.3. Note that the joule heating drops to zero by z = 1 cm. This plot shows a large amount of joule heating occurring near the cathode, with the RR 3.4 case having the most joule heating. This behavior matches Figures 6.1 and 6.2, as the higher total enthalpy for the RR 3.4 case indicates more heating was performed.

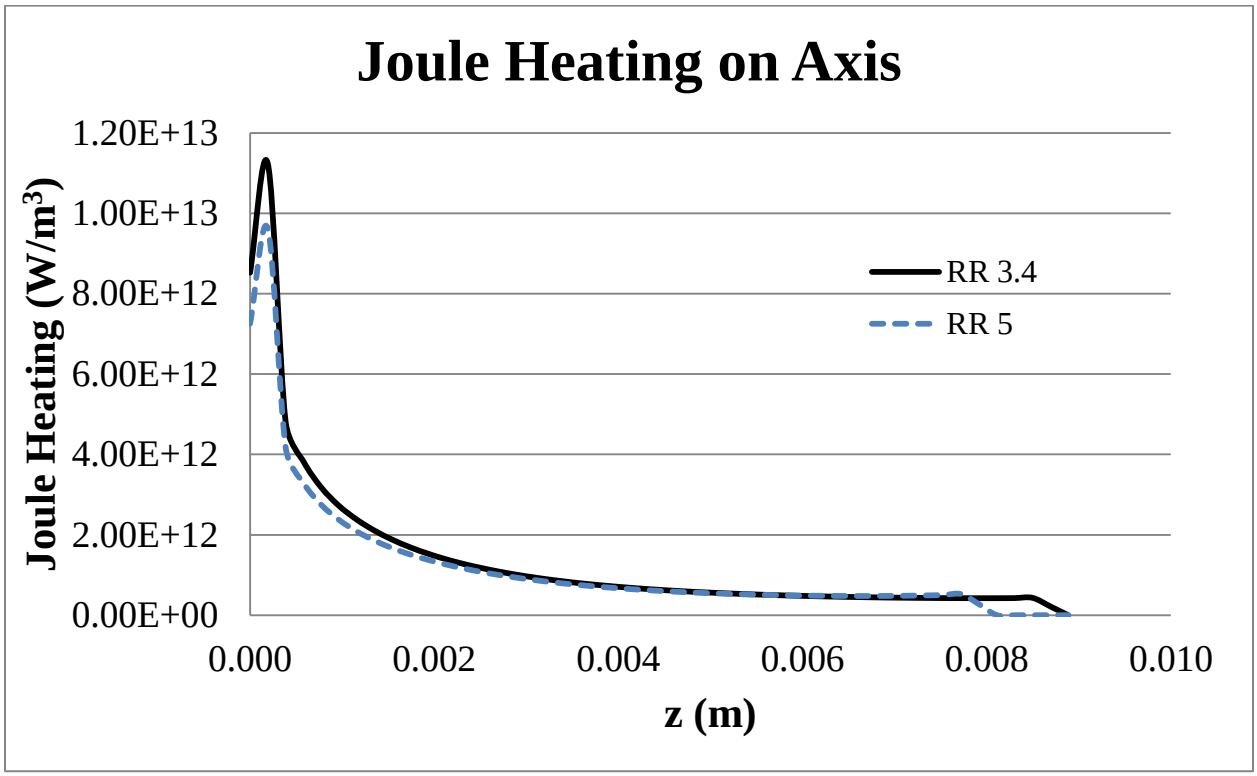


Figure 6.3: Joule heating along axis for both radius ratios.

## 6.3 Summary of Conclusions

1.) Using an axial integration method, the voltage for the radius ratio of 3.4 was shown to be 148 V, higher than the measured value of 130 V when accounting for the electrode sheaths. Additionally, the voltage for the radius ratio of 5 was shown to be 222 V.

2.) The simulated electron densities were lower than the experimental measurements, and the velocity values were higher. However, along the axis, the axial velocity was within the experimental error.

3.) The simulated magnetic field values matched very well the experimentally measured values taken at the face of the cathode and insulator.

4.) Along the axis, the radius ratio of 3.4 had a higher pressure up until the divergence of the anode (z = 9.3 mm), and past that point, the radius ratio of 5 had a higher pressure. The magnetic pressures at the cathode radius were equal for both cases. An electrothermal thrust component was indicated due to the pressure force at the cathode being higher than the predicted force which assumed only **j** x **B** effects.

5.) Compared to the experimental data, the electron temperature dropped quicker axially. This might have been due to the constant thermal conductivity. Additionally, the larger radius ratio case showed increased ion and electron temperatures.

6.) Conductivity results were shown, and the conductivity for the RR 3.4 case at z = 3.3 cm was shown to be higher than expected, though this was likely due to a difference between the predicted and MACH2 charge states. The conductivity for the RR 5 case was shown to be higher than that of the RR 3.4 case.

7.) Mass flow rates of 6 g/s were achieved for both radius ratios, though there might have been some error due to boundary conditions and to adding an insulator mass flow.

8.) The momentum flow rate was measured to be 124 N for the radius ratio of 3.4 and 131 N for the radius ratio of 5. These values were higher than predicted using the **j** x **B** derivation, however this difference of 7 N was smaller than the 19 N difference expected. These momentum flow rate results indicated the presence of an electrothermal

component of thrust, which was demonstrated through the heating near the cathode. Computational difficulties involved with setting the boundary conditions might have also had an effect on the momentum flow rate values.

9.) Efficiencies of 38% and 28% were calculated for the radius ratios of 3.4 and 5, respectively.

## 6.4 Avenues of Future Work

1.) Implementing a gallium equation of state would lead to more accurate results, in contrast to the ideal gas model used in this study.

2.) Implementing a gallium Saha equation would also better simulate the experiments instead of the constant ionization state model.

3.) Changing the thermal conductivity model from a constant value might lead to temperatures that do not drop as quickly axially.

4.) It might be beneficial to determine how to get the boundary condition output values to better match input values, in contrast to the "knob" approach used in this study. This might require examining methods of setting up the magnetic field without requiring extra blocks.

5.) Given that the mass flow did not extend out to the anode radius without adding an insulator mass flow, it would be beneficial to determine the maximum radius ratio that could be achieved experimentally in the GEM thruster. At a certain set anode radius, the flow from the cathode would not extend fully out, and thus the performance would not increase further.

# References


[1] Burton, R. L., K. E. Clark, and R. G. Jahn. "Measured Performance of a Multimegawatt MPD Thruster." *Journal of Spacecraft and Rockets* Vol. 20, No. 3, pp. 299-304, 1983.

[2] Jahn, Robert George. *Physics of Electric Propulsion*. Mineola, NY: Dover Publ., 1996.

[3] Gilland, James, Melissa McGuire, Tyacie Corle, and Michelle Clem. "Mission Performance of High-Power Electromagnetic Thruster Systems." *AIP Conference Proceedings*. Space Technology and Applications International Forum, Albuquerque, NM. Vol. 813, pp. 201-208, doi 10.1063/1.2169196, 2006.

[4] Gilland, James, Douglas Fiehler, and Valerie Lyons. "Electric Propulsion Concepts Enabled by High Power Systems for Space Exploration." Proc. of 2nd International Energy Conversion Engineering Conference, Providence, RI. AIAA 2004-5690, 2004.

[5] Polzin, Kurt A., Thomas E. Markusic, Rodney L. Burton, Robert E. Thomas, and David L. Carroll. "Gallium Electromagnetic (GEM) Thruster Concept and Design." Proc. of 42nd AIAA/ASME/SAE/ASEE Joint Propulsion Conference & Exhibit, Sacramento, CA. AIAA 2006-4652, 2006.

[6] Thomas, Robert E. "Development and Testing of a Gallium Electromagnetic (GEM) Thruster." PhD thesis, Dept. of Aerospace Engineering, University of Illinois, 2010.

[7] Thomas, Robert E., Rodney L. Burton, and Kurt A. Polzin. "Investigation of a Gallium MPD Thruster with an Ablating Cathode." AIAA-2010-6529, 2010.

[8] Thomas, Robert E., Rodney L. Burton, and Kurt A. Polzin. "Performance Characteristics of an Ablative Gallium Electromagnetic Accelerator." Submitted for publication.

[9] Mikellides, Pavlos. "Modeling and Analysis of a Megawatt-Class Magnetoplasmadynamic Thruster." *Journal of Propulsion and Power* Vol. 20, No. 2, pp.204-10, March-April 2004.

[10] Mikellides, Pavlos G. "Design and Operation of MW-Class MPD Thrusters Part I: Numerical Modeling." Proc. of 27th International Electric Propulsion Conference, Pasadena, CA. IEPC-01-124, 2001.

[11] Mikellides, Pavlos G., Norman F. Roderick, and Peter J. Turchi. "Applied-Field Magnetoplasmadynamic Thrusters, Part 1: Numerical Simulations Using the MACH2 Code." *Journal of Propulsion and Power* Vol. 16, No. 5, pp. 887-93, Sept.-Oct. 2000.

[12] LaPointe, Michael R., James H. Gilland, and Pavlos G. Mikellides. "High Power Electromagnetic Thrusters for Spacecraft Propulsion." Proc. of ASME International Mechanical Engineering Congress & Exposition, New Orleans, LA. IMECE2002-39354, Nov. 2002.

[13] Henrikson, Erik M., and Pavlos G. Mikellides. "Modeling of Ablation-Fed Pulsed Plasma Thruster Operation Using a New Approach to the Ablation Process." Proc. of 44th AIAA/ASME/SAE/ASEE Joint Propulsion Conference & Exhibit, Hartford, CT. AIAA 2008-4645, July 2008.

[14] Henrikson, Erik M., Pavlos G. Mikellides, and Hani Kamhaw. "Experimental and Numerical Characterization of an Ablation-fed Pulsed Plasma Thruster Prototype." Proc. of 31st International Electric Propulsion Conference, University of Michigan, Ann Arbor, MI. IEPC-2009-246, Sept. 2009.

[15] Cassibry, J., Thomas Markusic, Francis Thio, and S. Wu. "Numerical Modeling of a Pulsed Electromagnetic Plasma Thruster Experiment." *Journal of Propulsion and Power* Vol. 22, No. 3, pp. 628-36, 2006.

[16] Cassibry, J. T., T. E. Markusic, and S. T. Wu. "Effects of Propellant Injection, Material and Electrode Geometry on the Performance of a Two-Stage Pulsed Plasma Accelerator." Proc. of 40th AIAA/ASME/SAE/ASEE Joint Propulsion Conference and Exhibit, Fort Lauderdale, FL. AIAA 2004-2361, July 2004.

[17] Mikellides, Pavlos G. and Michael R. LaPointe. "Magnetohydrodynamic MACH Code Used to Simulate Magnetoplasmadynamic Thrusters." NASA technical document. 2002.

[18] Peterkin, Robert E., Michael H. Frese, and Carl R. Sovinec. "Transport of Magnetic Flux in an Arbitrary Coordinate ALE Code." *Journal of Computational Physics* Vol. 140, No. 1 pp. 148-71, 1998.